https://doi.org/10.1088/1751-8121/aaabc6

Bounds on quantum collapse models from matter-wave interferometry: calculational details

Marko Toroš[1,3] **and Angelo Bassi**[2]

[1] Department of Physics, University of Trieste, 34151 Miramare-Trieste, Italy
[2] Istituto Nazionale di Fisica Nucleare, Sezione di Trieste, Via Valerio 2, 34127 Trieste, Italy

E-mail: marko.toros@ts.infn.it and bassi@ts.infn.it

Accepted for publication 31 January 2018

Abstract

We present a simple derivation of the interference pattern in matter-wave interferometry predicted by a class of quantum master equations. We apply the obtained formulae to the following collapse models: the Ghirardi–Rimini–Weber (GRW) model, the continuous spontaneous localization (CSL) model together with its dissipative (dCSL) and non-Markovian generalizations (cCSL), the quantum mechanics with universal position localization (QMUPL), and the Diósi–Penrose (DP) model. We discuss the separability of the dynamics of the collapse models along the three spatial directions, the validity of the paraxial approximation, and the amplification mechanism. We obtain analytical expressions both in the far field and near field limits. These results agree with those already derived in the Wigner function formalism. We compare the theoretical predictions with the experimental data from two recent matter-wave experiments: the 2012 far-field experiment of Juffmann T *et al* (2012 *Nat. Nanotechnol.* **7** 297–300) and the 2013 Kapitza–Dirac–Talbot–Lau (KDTL) near-field experiment of Eibenberger *et al* (2013 *Phys. Chem. Chem. Phys.* **15** 14696–700). We show the region of the parameter space for each collapse model that is excluded by these experiments. We show that matter-wave experiments provide model-insensitive bounds that are valid for a wide family of dissipative and non-Markovian generalizations.

Keywords: matter-wave interferometry, spontaneous collapse models, superposition principle, quantum foundations, macromolecules

(Some figures may appear in colour only in the online journal)

1. Introduction

The interest in exploring the foundations of quantum mechanics has significantly increased over the years. This applies both to theoretical foundations and experimental foundations. After the establishment of quantum nonlocality, first with the works of Bell [3, 4] and subsequently with the experimental confirmation done by the group of Aspect [5–7], perhaps the most important question is whether the so-called collapse of the wave function is a physical phenomenon.

Quantum mechanics also allows for the possibility that macroscopic objects—being made of atoms, which are quantum—might live in the superpositions of different states. But this has never been observed. Why so? Is it simply because macroscopic quantum superpositions are difficult to spot, due to environmental noises, or because they are forbidden for some physical reason? No one knows the answer yet, and research is active in testing which of the two alternatives is correct.

Collapse models [8, 9] have been formulated to take this second possibility into account: nature forbids macroscopic systems to live in superposition states. From the mathematical point of view, the Schrödinger equation is modified by adding nonlinear and stochastic terms, which account for the quantum-to-classical transition. For microscopic systems, the standard quantum evolution is the dominant contribution to the dynamics, hence they behave in a fully quantum way, as repeatedly confirmed in experiments. For macroscopic objects, on the other hand, the opposite is true: the nonlinear terms prevent superpositions to occur. The border between these two regimes lies somewhere in the mesoscopic world.

As such, collapse models are predictively different from standard quantum mechanics, and research is active in testing them [9], because any test of collapse models is a test of the quantum superposition principle, which lies at the foundations of any quantum theory.

Different collapse models have been proposed over the years. The most famous model is the continuous spontaneous localisation (CSL) model [10, 11], a generalisation of the original Ghirardi–Rimini–Weber (GRW) model [12] to systems containing identical particles. The CSL model, in the limit of short superposition distances, reduces to the quantum mechanics with universal position localization (QMUPL) model [13, 14]. In all cases, the noise driving the collapse is a white noise. This modelling of the noise is very useful from the practical point of view, as in this case the equations of motions are relatively simple, however a white noise is not physical. For this reason, in recent years the CSL model has been generalised in two directions. On the one side, dissipative effects have been included in the dynamics, which drive any quantum system, during the collapse, to a thermal state. This partly solves the problem of the steady energy increases, which affects the CSL model. The model is called the dissipative CSL (dCSL) model [15]. Its limiting case, the dissipative QMUPL model, has also been studied [16]. On the other hand, the white noise has been replaced by a coloured noise [17–19]. In this case we speak of coloured CSL (cCSL). A coloured noise introduces non-Markovian terms in the dynamics, making the whole mathematical analysis rather difficult. The cCSL model reduces to the coloured QMUPL model in the limit of short superposition distances [20]. Only for the QMUPL model, both dissipative and non-Markovian effects have been combined together in a single model [21], so far. Independent from the CSL model, there is the Diosi–Penrose (DP) model [13], which is a first attempt to link the collapse of the wave function to gravity.

All these models contain phenomenological parameters. The GRW and CSL models are defined in terms of a localization rate λ and a localization length r_C. λ gives the frequency of the localization events for a reference object of mass $m_0 = 1$ amu, while r_C describes how well an object is localized. The QMUPL model has only the parameter η, which can be related to

the GRW/CSL parameters [22]. A common open question of both the GRW and CSL models, is to explain the origin of the noise in the dynamical equations. A first attempt at addressing this issue is given by the DP model, where the strength of the localization is set by the gravitational interaction through the gravitational constant G. The DP model introduces only one cut-off length phenomenological parameter R_0, which cures the ultraviolet divergence of the gravitational interaction. The effective collapse rate, analogous to λ, is given by $Gm_0^2/\sqrt{\pi}\hbar R_0$, while R_0 describes how well an object is localized, analogous to r_C.

One unwanted feature, common to the GRW, CSL and DP models, is the energy divergence for very long (cosmological) times. Indeed, the GRW, CSL and DP master equations have the structure of a quantum linear Boltzmann equation [23] of a particle immersed in a infinite temperature bath. One attempt to solve this issue, is proposed by the dissipative extensions of the GRW and CSL models, namely the dGRW and dCSL models, respectively [15, 24]. Here the energy divergence is eliminated by the introduction of a noise temperature parameter T. Another approach to solve the energy divergence, adopted by the cCSL model [18, 19], is to replace the non-physical white noise by a colored noise with a finite correlation time parameter τ_C. We provide a brief summary of the former these models in section 3. Alternatively, instead of the position-based collapse models introduced above, one can also consider the class of energy-based collapse models, which localize in energy eigenstates, and preserve the energy of an isolated system. In this paper, we limit the discussion to the former ones and refer the reader interested in the latter ones to [25–30].

Bounds on collapse models parameters are first investigated in [31] and an overview is given in [32, 33]. In this paper, we complete and improve the previous analysis of collapse models' predictions for matter-wave interferometry. The bounds on the parameters (λ, r_C) can be conveniently studied in the parameter space [34, 35] shown in figure 13, while the bounds on the parameters η are shown in figures 14. We obtain bounds for all the collapse models introduced above, from the localization requirement of macroscopic objects and from experimental data.

We describe how to obtain the bounds from the localization requirement of macroscopic objects at the end of section 4, where we discuss a key feature of all collapse models, namely the amplification of the effective collapse rate, as the size (mass) of the system increases. In other words, under standard assumptions, the center of mass motion for a rigid many-body system is governed by the single particle equation with a rescaled collapse rate.

We show that, on the one hand, current matter-wave experiments do not give significant bounds on the DP parameter R_0, while, on the other hand, the localization requirement of macroscopic objects (as defined in sections 4 and 5), excludes all values of R_0.

The first and main prediction of collapse models is the gradual modification of the interference pattern in interferometric experiments, as the mass of the diffracted object becomes large. Therefore matter-wave experiments provide the most direct test of collapse models. They are described in sections 2 and 5. In particular, in section 2 we derive the interference pattern $p(x)$ for the experimental setup described in figure 1. We compare the theoretical interference patterns with experimental data from the 2012 far-field matter-wave interferometry experiment [1, 36] and the 2013 Kapitza–Dirac–Talbot–Lau (KDTL) near-field matter-wave interferometry experiment [2], in section 5. Tests of the CSL model with matter-wave interferometry experiments were first investigated in [31, 37], in particular, in the context of the OTIMA experiment [38]. In a recent publication [39], we have presented the matter-wave interferometry bounds for the CSL model and its variants, here discussed. In this paper we give the full derivations of formulas, which were presented, without derivation, in the publication [39].

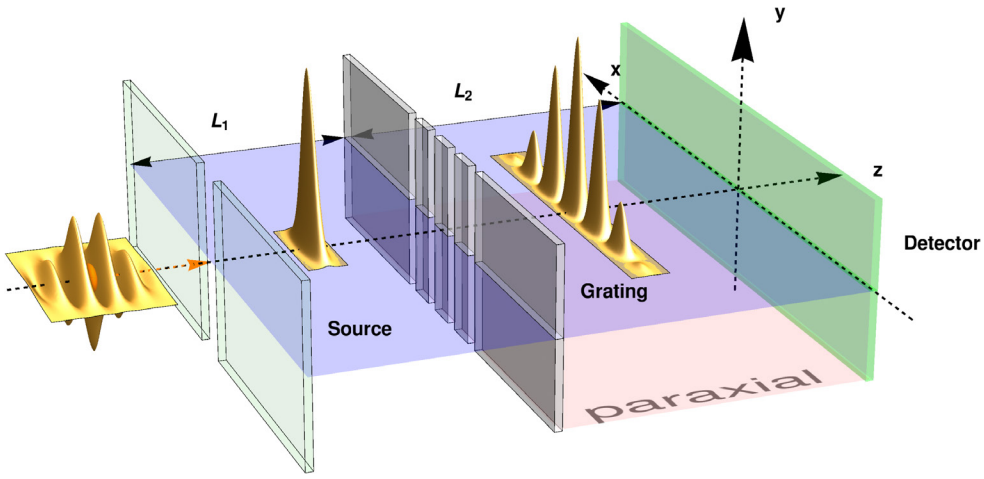

Figure 1. The common structure of far-field and near-field diffraction experiments. A molecular beam from an incoherent source propagates along the z axis. Each molecule is emitted from the source, propagates to the grating, where it is diffracted and then recorded by the detector. The molecules individually recorded gradually form an interference pattern. The figure shows a mechanical grating (with $N = 4$ slits), but the analysis in this paper applies to more general gratings, e.g. optical gratings. The distance from the source to the grating is L_1 and the distance from the grating to detector is L_2. Between the grating and the detector we identify the paraxial (Fresnel) regime. Adapted from [39], Copyright (2017), with permission from Elsevier.

The interference pattern derived in section 2 in the density matrix formalism is not limited only to collapse models, but is valid for a large class of dynamics. In particular, we also discuss under which conditions the diffraction experiment can be reduced to a one dimensional problem, since the collapse dynamics, unlike ordinary quantum mechanics, is not separable in the three spatial dimension, even for the free particle dynamics. In this way we justify the calculation of the interference pattern in the paraxial approximation. In addition, the density matrix formalism outlines the similarities of far-field and near-field interference, by presenting a unified derivation. We also reobtain the results for diffraction experiments that were derived in the Wigner function formalism [38, 40, 41].

In section 5 we combine all the parameter bounds for the CSL, GRW, dCSL, dGRW and cCSL models in a single parameter diagram and we discuss the bounds on the parameter of the QMUPL model as well as on the length parameter of the DP model.

2. Derivation of the interference pattern

For all collapse models considered here (see the next section), the evolution of the free single-particle density matrix has the form:

$$\rho(\boldsymbol{x},\boldsymbol{x}',t) = \frac{1}{(2\pi\hbar)^3}\int \mathrm{d}\tilde{\boldsymbol{k}}\int \mathrm{d}\tilde{\boldsymbol{w}}\ \mathrm{e}^{-\frac{\mathrm{i}}{\hbar}\tilde{\boldsymbol{k}}\cdot\tilde{\boldsymbol{w}}}F(\tilde{\boldsymbol{k}},\boldsymbol{x}-\boldsymbol{x}',t)\rho^{\mathrm{QM}}(\boldsymbol{x}+\tilde{\boldsymbol{w}},\boldsymbol{x}'+\tilde{\boldsymbol{w}},t), \tag{1}$$

where ρ^{QM} is the free standard quantum mechanical density matrix and the function F depends on the type of collapse model.

The quantum mechanical description of matter-wave interferometry is usually treated as a one-dimensional problem. This is justified by the fact that the free Schrödinger dynamics is separable along the three directions of motion. On the contrary, in general the dynamics given by equation (1) is not separable, not even in the free particle case. We show, however, that due to the specific geometry and experimental parameters of the diffraction experiments here considered, we can effectively separate the collapse dynamics in the three spatial directions, thus considerably simplifying the problem. Along with this, we will investigate the assumptions that are required for the justification of the one dimensional approximation. Actually, it is instructive to first carry out the calculation in the 1D (paraxial) approximation before justifying it.

The derivation of the paraxial interference pattern is the main result of this section. We then apply the paraxial interference formula to the far-field and near-field experimental setups. In order to simplify the comparison with similar results obtained in the literature, we will adopt the notation of [42]. We will also omit the overall normalization factors for the wave functions, density matrices and probability densities. At any step of the calculation, one can obtain a normalized quantity by dividing with an appropriate normalization factor.

2.1. Paraxial approximation

We first review the quantum mechanical derivation of the interference pattern in the paraxial (Fresnel) region, as depicted in figure 1. We label with z_1, z_2, z_3 the positions of source, grating and detector along the optical axis z, respectively. Similarly, we label the horizontal coordinates along the optical elements as x_1, x_2, x_3, respectively.

In the paraxial diffraction region the evolution of the wave function can be approximated by the free quantum mechanical wave function propagation in one spatial dimension, i.e. the Fresnel diffraction integral:

$$\psi(x; t = L/v) = \int_{-\infty}^{+\infty} \mathrm{d}x_0 \psi_0(x_0)\, \mathrm{e}^{\frac{\mathrm{i}k}{2L}(x-x_0)^2}, \tag{2}$$

where k is the wave number of the matter wave, ψ_0 is the initial wave function and ψ is the wave function after it has propagated for a distance L in a time $t = L/v$, where v is the speed of propagation along the optical axis z. One has the usual relation $mv = \hbar k$, where m is the mass of the system (the macromolecule). In the language of density matrices equation (2) reads:

$$\rho^{\mathrm{QM}}(x, x'; t = L/v) = \int_{-\infty}^{+\infty} \mathrm{d}x_0' \int_{-\infty}^{+\infty} \mathrm{d}x_0 \rho_0(x_0, x_0')\, \mathrm{e}^{\frac{\mathrm{i}k}{2L}((x-x_0)^2-(x'-x_0')^2)}, \tag{3}$$

where $\rho_0(x_0, x_0')$ is the initial density matrix and $\rho^{\mathrm{QM}}(x, x'; t)$ is the density matrix after it has propagated for a distance L in a time $t = L/v$.

The calculation of the interference pattern can be summarized in the following steps.

[z_1]: We choose the initial wave function at z_1. Both the far-field and near-field experiments will be modeled by a completely incoherent source at z_1, meaning that the wave functions associated to different molecules are uncorrelated and spatially localized initially. It is then sufficient to consider a single source at point (x_1, z_1). At the end, one can integrate over the extension of the source. The corresponding initial wave function is given by

$$\psi_1(\tilde{x}_1) = \delta(x_1 - \tilde{x}_1). \tag{4}$$

[z_1 to z_2]: We propagate the wave function to z_2 according to equation (2):

$$\psi_2(x_2) = \int_{-\infty}^{+\infty} \mathrm{d}\tilde{x}_1 \psi_1(\tilde{x}_1)\, \mathrm{e}^{\frac{\mathrm{i}k}{2L_1}(x_2-\tilde{x}_1)^2}. \tag{5}$$

[z_2]: We now assume that the optical element at position z_2 has a transmission function $t(x)$. The wave function immediately after the grating at z_2 is given by $t(x_2)\psi_2(x_2)$.

[z_2 to z_3]: We propagate the wave function from z_2 to z_3 according to equation (2):

$$\psi_3(x_3) = \int_{-\infty}^{+\infty} \mathrm{d}x_2 t(x_2)\psi_2(x_2)\, \mathrm{e}^{\frac{\mathrm{i}k}{2L_2}(x_3-x_2)^2}. \tag{6}$$

[z_3]: The detector records the arrival of the molecules along the axis x_3. The probability distribution is $p_3(x_3) = |\psi_3(x_3)|^2$. After combining the equations of the previous steps we obtain the interference pattern:

$$\begin{aligned} p_3(x_3) = \int_{-\infty}^{+\infty} \mathrm{d}x_2 \int_{-\infty}^{+\infty} \mathrm{d}x_2' t(x_2)t^*(x_2') \\ \mathrm{e}^{-\frac{\mathrm{i}k}{2L_2}(x_2-x_2')x_3}\, \mathrm{e}^{\frac{\mathrm{i}k}{2L_1}(x_2^2-x_2'^2)}\, \mathrm{e}^{\frac{\mathrm{i}k}{2L_2}(x_2'^2-x_2^2)}\, \mathrm{e}^{-\frac{\mathrm{i}k}{L_1}(x_2-x_2')x_1}. \end{aligned} \tag{7}$$

Note that equation (7) was derived from equation (2), but it could equally well be derived from the density matrix evolution given by equation (3).

We now consider what happens if in place of the standard quantum evolution, we have the following density matrix evolution:

$$\rho(x,x';t) = \frac{1}{2\pi\hbar}\int_{-\infty}^{+\infty} \mathrm{d}\tilde{k} \int_{-\infty}^{+\infty} \mathrm{d}\tilde{w}\ \mathrm{e}^{-\frac{\mathrm{i}}{\hbar}\tilde{k}\tilde{w}} F(\tilde{k},0,0;x-x',0,0;t)\rho^{\mathrm{QM}}(x+\tilde{w},x'+\tilde{w};t). \tag{8}$$

We will justify equation (8) below, when we discuss the separability issue. The calculation of the interference pattern can be again carried out as before.

[z_1]: We consider a single source at point (x_1, z_1). The corresponding initial wave function is given by $\psi_1(\tilde{x}_1) = \delta(x_1 - \tilde{x}_1)$ and the corresponding density matrix is given by

$$\rho_1(\tilde{x}_1,\tilde{x}_1') = \delta(x_1-\tilde{x}_1)\delta(x_1-\tilde{x}_1'). \tag{9}$$

[z_1 to z_2]: We propagate the density matrix from the point z_1 to the point z_2 along the optical axis using equation (8):

$$\rho_2(x_2,x_2) = \frac{1}{2\pi\hbar}\int_{-\infty}^{+\infty} \mathrm{d}\tilde{k} \int_{-\infty}^{+\infty} \mathrm{d}\tilde{w}\ \mathrm{e}^{-\frac{\mathrm{i}}{\hbar}\tilde{k}\tilde{w}} F(\tilde{k},0,0;x-x',0,0;t)\rho_2^{\mathrm{QM}}(x_2+\tilde{w},x_2'+\tilde{w}), \tag{10}$$

where according to equations (3) and (9):

$$\rho_2^{\mathrm{QM}}(x_2,x_2') = \mathrm{e}^{\frac{\mathrm{i}k}{2L_1}(x_2^2-x_2'^2)}\, \mathrm{e}^{-\frac{\mathrm{i}k}{L_1}(x_2-x_2')x_1}. \tag{11}$$

In equation (10) the $\tilde{w}$ integration yields a delta function $\delta(\tilde{k} - \frac{\hbar k}{L_1}(x_2 - x_2'))$ and hence after the $\tilde{k}$ integration we obtain:

$$\rho_2(x_2,x_2') = \mathrm{e}^{\frac{\mathrm{i}k}{2L_1}(x_2^2-x_2'^2)}\, \mathrm{e}^{-\frac{\mathrm{i}k}{L_1}(x_2-x_2')x_1} F\left(\frac{\hbar k}{L_1}(x_2-x_2'),0,0;x_2-x_2',0,0;t_1\right). \tag{12}$$

[z_2]: We apply the grating's transmission function $t(x)$ to the density matrix and obtain $t(x_2)\rho_2(x_2,x_2')t^*(x_2')$.

[z_2 to z_3]: We perform a free propagation according to equation (8) from z_2 to z_3:

$$\rho_3(x_3,x_3') = \frac{1}{2\pi\hbar}\int_{-\infty}^{+\infty} \mathrm{d}\tilde{k} \int_{-\infty}^{+\infty} \mathrm{d}\tilde{w}\ \mathrm{e}^{-\frac{\mathrm{i}}{\hbar}\tilde{k}\tilde{w}} F(\tilde{k},0,0;x_3-x_3',0,0;t_2)\rho_3^{\mathrm{QM}}(x_3+\tilde{w},x_3'+\tilde{w}) \tag{13}$$

where

$$\rho_3^{\mathrm{QM}}(x_3,x_3') = \int_{-\infty}^{+\infty} \mathrm{d}x_2 \int_{-\infty}^{+\infty} \mathrm{d}x_2'\, t(x_2)t^*(x_2')\rho_2(x_2,x_2')\ \mathrm{e}^{\frac{\mathrm{i}k}{2L_2}((x_3-x_2)^2-(x_3'-x_2')^2)}. \tag{14}$$

[z_3]: The interference pattern is again proportional to the probability density $p(x) = \rho_3(x,x)$. The $\tilde{w}$ integration yields a delta function $\delta(\tilde{k} + \frac{\hbar k}{L_2}(x_2 - x_2'))$. Hence after the $\tilde{k}$ integration we obtain the interference pattern:

$$\begin{aligned} p(x) = &\int_{-\infty}^{+\infty} \mathrm{d}x_2 \int_{-\infty}^{+\infty} \mathrm{d}x_2'\, D(x_2-x_2')\ t(x_2)t^*(x_2') \\ &\times\ \mathrm{e}^{-\mathrm{i}\frac{mv}{\hbar}(x_2-x_2')(\frac{x_1}{L_1}+\frac{x}{L_2})}\ \mathrm{e}^{\mathrm{i}\frac{mv}{\hbar}\frac{L_1+L_2}{2L_1L_2}(x_2^2-x_2'^2)}, \end{aligned} \tag{15}$$

where

$$D(x_2-x_2') = F(-\frac{\hbar k}{L_2}(x_2-x_2'),0,0;0,0,0;t_2)F(\frac{\hbar k}{L_1}(x_2-x_2'),0,0;(x_2-x_2'),0,0;t_1). \tag{16}$$

As we can see, the interference pattern in equation (15) differs from the pure quantum mechanical interference pattern of equation (7) by the presence of $D(x_2 - x_2')$.

2.2. Separability

We now perform the full 3D treatment of the problem to justify the 1D approximation. We consider an initial Gaussian wave packet, evolving according to the full dynamics in equation (1). For the geometry, we refer again to the experimental setup depicted in figure 1. We will show under which assumptions the interference pattern is given by equation (15), thus justifying the above analysis in the 1D (paraxial) approximation. The assumptions are:

1: The extension of the macromolecule $\sigma(t)$ is much smaller then the distances L_1, L_2 during the time of flight t:

$$\sigma(t) \ll L_1, L_2. \tag{17}$$

This key assumption allows to split the flight of the molecule from the source at time $t = 0$ to the grating at time t_1, from the motion from the grating at time t_1 to the detector at time $t_1 + t_2$, and to treat the non-free interaction with the grating as instantaneous. This is necessary in order to conveniently introduce a transmission function for the grating $t_{xy}(x,y)$. In particular, we choose $t_{xy}(x,y) = t(x)t_y(y)$, where

$$t(x) = 0 \quad \text{if } |x| > \frac{s_x}{2}, \tag{18}$$

while for $|x| < \frac{s_x}{2}$ it depends on the type of grating and

$$t_y(y) = \begin{cases} 1, & \text{if } |y| \leqslant \frac{s_y}{2}. \\ 0, & \text{if } |y| > \frac{s_y}{2}. \end{cases} \tag{19}$$

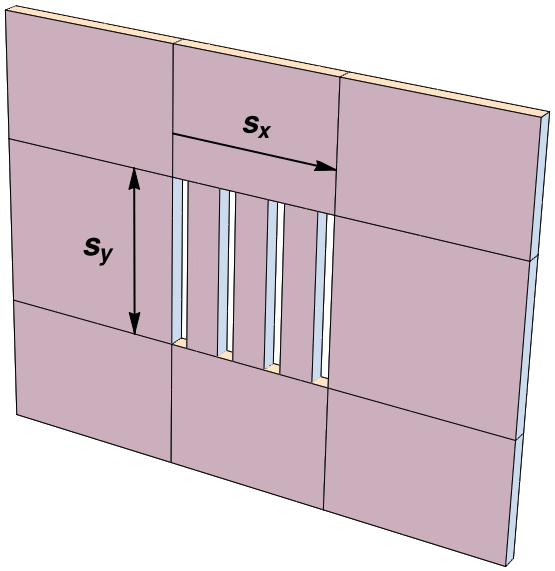

Figure 2. The grating has non-zero transmission function limited to a rectangle of size $s_x \times s_y$, e.g. here we show a mechanical grating with $N = 4$ slits with total horizontal extension s_x and slit height s_y. The analysis of this section applies also to other types of gratings, e.g. an optical grating.

where s_x, s_y are described in figure 2 and $t(x)$ is to be identified with the transmission function used above, when working in the 1D (paraxial) approximation.

2: We assume that the molecule extension σ_2 at time t_1, as it reaches the grating, is much larger than the molecule extension σ_1, at time $t = 0$, as it leaves the source:

$$\sigma_1 \ll \sigma_2. \tag{20}$$

3: We require that the grating transmission function satisfies (see figure 2):

$$s_x \ll \sigma_2, \tag{21}$$
$$\sigma_2 \ll s_y. \tag{22}$$

Using ordinary quantum mechanics it is easy to give an estimate for the molecule extension at the grating: $\sigma_2 = \frac{\hbar t_1}{m\sigma_1}$ with σ_1 the extension at the source (see analysis below). Using this relation let us check the validity of the above assumptions for the two experiments considered.

For the far-field diffraction experiment [36] we have $L_1 = 0.702$ m, $L_2 = 0.564$ m, $s_x = 3\mu$m, $s_y = 60\mu$m and the molecular speed along the z axis $v \sim 100$ ms^{-1}. The above assumptions are satisfied if the initial molecular extension at the source is contained in the interval 4×10^{-9} m $\lesssim \sigma_1 \lesssim 7 \times 10^{-8}$ m. No one knows the actual value of σ_1. The range of values here considered makes the initial spread much smaller than the extension of the source ($s = 1\mu$m) as given by the collimator and also provides a justification as to why the source is incoherent.

For the near-field KDTL diffraction experiment [2] we have $L_1 = L_2 = 10.5$ cm, while it is difficult to give estimates for parameters s_x, s_y of the light grating. Anyhow, making

the following guess for these parameters: $s_x = 10^{-3}$ m, $s_y = 100 \times 10^{-3}$ m (and being the molecular speed along the z axis $v \sim 100$ ms^{-1}), the above assumptions are satisfied if the initial molecular extension at the source is contained in the interval 10^{-13} m $\lesssim \sigma_1 \lesssim 10^{-11}$ m. This is to be compared with the slit openings of the source grating $l = 110$ nm. Without more precise estimates for the molecule extension $\sigma(t)$ it is difficult to assess the validity of the above assumptions and hence of the 1D approximation. We stress that we are considering a single molecule emitted from the source. In particular, the single molecule extension $\sigma(t)$ should not be confused with the spatial coherence length of the beam, which is a property of an ensemble of particles emitted from the source.

As in the previous section, the calculation of the interference pattern can be split into several steps.

[z_1]: It is convenient to work in a boosted reference frame along the z axis with molecular velocity v, i.e. moving alongside the molecule. For non boost-invariant dynamics, one has to choose the correct function F depending on the reference frame. To simplify the analysis we neglect gravity and we consider an initial Gaussian wave-function centered at (x_1,0,0):

$$\psi_1(\tilde{x}_1, \tilde{y}_1, \tilde{z}_1) = \mathrm{e}^{-\frac{(x_1-\tilde{x}_1)^2}{4\sigma_1^2}} \mathrm{e}^{-\frac{\tilde{y}_1^2}{4\sigma_1^2}} \mathrm{e}^{-\frac{\tilde{z}_1^2}{4\sigma_1^2}}, \tag{23}$$

with the corresponding density matrix given by

$$\rho_1(\tilde{x}_1, \tilde{y}_1, \tilde{z}_1; \tilde{x}_1', \tilde{y}_1', \tilde{z}_1') = \psi_1(\tilde{x}_1, \tilde{y}_1, \tilde{z}_1)\psi_1^*(\tilde{x}_1', \tilde{y}_1', \tilde{z}_1'). \tag{24}$$

[z_1 to z_2]: We propagate the density matrix ρ_1 from $t = 0$ to $t = t_1 = L_1/v$ using equation (1). We denote the resulting density matrix as $\rho_2(x_2, y_2, z_2; x_2', y_2', z_2')$ (and by $\rho_2^{\mathrm{QM}}(x_2, y_2, z_2; x_2', y_2', z_2')$ the quantum mechanical evolution of ρ_1 at $t = t_1$). In particular, using the separability of ordinary quantum mechanics, the quantum mechanical wave function just before t_1 is given by:

$$\psi_2^{\mathrm{QM}}(x_2, y_2, z_2) = \psi_2^{\mathrm{QM}(1)}(x_2; x_1)\psi_2^{\mathrm{QM}(1)}(y_2; 0)\psi_2^{\mathrm{QM}(1)}(z_2; 0), \tag{25}$$

where $\psi_2^{\mathrm{QM}(1)}(x_2; x_1) = \exp\left[-\frac{(x_2-x_1)^2}{4\sigma_1^2(1+\frac{\mathrm{i}\hbar t_1}{2m\sigma_1^2})}\right]$. Hence the quantum mechanical density matrix is given by:

$$\rho_2^{\mathrm{QM}}(x_2, y_2, z_2; x_2', y_2', z_2'; t_1) = \rho_2^{\mathrm{QM}(1)}(x_2, x_2'; x_1)\rho_2^{\mathrm{QM}(1)}(y_2, y_2'; 0)\rho_2^{\mathrm{QM}(1)}(z_2, z_2'; 0), \tag{26}$$

where

$$\begin{aligned}\rho_2^{\mathrm{QM}(1)}(x, x', x_1) = \exp\Big[-\frac{1}{\sigma_2^2}\Big(& x^2\Big(1 - \frac{\mathrm{i}\hbar t_1}{2m\sigma_1^2}\Big) + x'^2\Big(1 + \frac{\mathrm{i}\hbar t_1}{2m\sigma_1^2}\Big) \\ & - 2xx_1\Big(1 + \frac{\mathrm{i}\hbar t_1}{2m\sigma_1^2}\Big) - 2x'x_1\Big(1 - \frac{\mathrm{i}\hbar t_1}{2m\sigma_1^2}\Big) + 2x_1^2\Big)\Big]\end{aligned} \tag{27}$$

and $\sigma_2 = \frac{\hbar t_1}{m\sigma_1}$ because of equation (20), i.e. $\frac{\hbar^2 t_1^2}{4m^2\sigma_1^4} \gg 1$. To summarize this step of the calculation:

$$\rho_2(x_2,y_2,z_2;x_2',y_2',z_2') = \int \mathrm{d}\tilde{k}_x \int \mathrm{d}\tilde{w}_x \rho_2^{\mathrm{QM}(1)}(x_2+\tilde{w}_x, x_2'+\tilde{w}_x; x_1)\, \mathrm{e}^{-\frac{\mathrm{i}}{\hbar}\tilde{k}_x\tilde{w}_x}$$
$$\times \int \mathrm{d}\tilde{k}_y \int \mathrm{d}\tilde{w}_z \rho_2^{\mathrm{QM}(1)}(y_2+\tilde{w}_y, y_2'+\tilde{w}_y; 0)\, \mathrm{e}^{-\frac{\mathrm{i}}{\hbar}\tilde{k}_y\tilde{w}_y}$$
$$\times \int \mathrm{d}\tilde{k}_z \int \mathrm{d}\tilde{w}_z \rho_2^{\mathrm{QM}(1)}(z_2+\tilde{w}_z, z_2'+\tilde{w}_z; 0)\, \mathrm{e}^{-\frac{\mathrm{i}}{\hbar}\tilde{k}_z\tilde{w}_z}$$
$$\times F(\tilde{k}_x,\tilde{k}_y,\tilde{k}_z; x_2-x_2', y_2-y_2', z_2-z_2'; t_1). \tag{28}$$

[z_2]: We apply the transmission function on the x and y axis given by equations (18) and (19) respectively. Let us first consider the integrals along the x axis. Using equation (21) we can simplify in equation (27) (which is contained in equation (28)):

$$\rho_2^{\mathrm{QM}(1)}(x,x',x_1)t(x)t^*(x') = \exp\left[-\frac{\mathrm{i}(-x^2+x'^2-2x_1(x-x'))\frac{\sigma_2}{2\sigma_1}}{\sigma_2^2}\right] t(x)t^*(x'). \tag{29}$$

The dependence on $\tilde{w}_x$, which will be integrated out, is contained in:

$$\mathrm{e}^{-\frac{\mathrm{i}}{\hbar}\tilde{k}_x\tilde{w}_x}\rho_2^{\mathrm{QM}(1)}(x_2+\tilde{w}_x; x_2'+\tilde{w}_x) = \exp\left[\frac{\mathrm{i}B(x_2,x_2')\tilde{w}_x}{\sigma_2^2}\right] \mathrm{Exp}\left[\frac{C(x_2,x_2')}{\sigma_2^2}\right], \tag{30}$$

where

$$B(x_2,x_2') = \frac{\sigma_2}{\sigma_1}(x_2-x_2') - \frac{1}{\hbar}\tilde{k}_x\sigma_2^2 \tag{31}$$

$$C(x_2,x_2') = \frac{\mathrm{i}\sigma_2}{2\sigma_1}\left((x_2^2-x_2'^2)+2x_1(x_2-x_2')\right). \tag{32}$$

Hence the $\tilde{w}_x$ integral yields the delta function $\delta(\tilde{k}_x-(x_2-x_2')\frac{m}{t_1})$, which we use to perform $\tilde{k}_x$ integration. On the y axis, by assumption (22), we can replace $t_y(y)$ by 1. To summarize, after performing the x-axis integrations we obtain:

$$\rho_2(x_2,y_2,z_2;x_2',y_2',z_2') = \mathrm{e}^{\frac{\mathrm{i}k}{2L_1}(x_2^2-x_2'^2)}\, \mathrm{e}^{-\frac{\mathrm{i}k}{L_1}(x_2-x_2')x_1}$$
$$\times \int \mathrm{d}\tilde{k}_y \int \mathrm{d}\tilde{w}_z \rho_2^{\mathrm{QM}(1)}(y_2+\tilde{w}_y, y_2'+\tilde{w}_y; 0)\, \mathrm{e}^{-\frac{\mathrm{i}}{\hbar}\tilde{k}_y\tilde{w}_y}$$
$$\times \int \mathrm{d}\tilde{k}_z \int \mathrm{d}\tilde{w}_z \rho_2^{\mathrm{QM}(1)}(z_2+\tilde{w}_z, z_2'+\tilde{w}_z; 0)\, \mathrm{e}^{-\frac{\mathrm{i}}{\hbar}\tilde{k}_z\tilde{w}_z}$$
$$\times F(\frac{\hbar k}{L_1}(x_2-x_2'),\tilde{k}_y,\tilde{k}_z; x_2-x_2', y_2-y_2', z_2-z_2'; t_1). \tag{33}$$

[z_2 to z_3]: We apply equation (1) to $\rho_2(x_2,y_2,z_2;x_2',y_2',z_2')$ for a time $t_2=\frac{L_2}{v}$:

$$\rho_3(x_3,y_3,z_3;x_3',y_3',z_3') = \int \mathrm{d}\tilde{\tilde{k}}_x \int \mathrm{d}\tilde{\tilde{w}}_x\, \mathrm{e}^{-\frac{\mathrm{i}}{\hbar}\tilde{\tilde{k}}_x\tilde{\tilde{w}}_x} \int \mathrm{d}\tilde{\tilde{k}}_y \int \mathrm{d}\tilde{\tilde{w}}_z\, \mathrm{e}^{-\frac{\mathrm{i}}{\hbar}\tilde{\tilde{k}}_y\tilde{\tilde{w}}_y}$$
$$\times \int \mathrm{d}\tilde{\tilde{k}}_z \int \mathrm{d}\tilde{\tilde{w}}_z\, \mathrm{e}^{-\frac{\mathrm{i}}{\hbar}\tilde{\tilde{k}}_z\tilde{\tilde{w}}_z} F(\tilde{\tilde{k}}_x,\tilde{\tilde{k}}_y,\tilde{\tilde{k}}_z; x_3-x_3', y_3-y_3', z_3-z_3'; t_2)$$
$$\times \rho_3^{\mathrm{QM}}(x_3+\tilde{\tilde{w}}_x, y_3+\tilde{\tilde{w}}_y, z_3+\tilde{\tilde{w}}_z; x_3'+\tilde{\tilde{w}}_x, y_3'+\tilde{\tilde{w}}_y, z_3'+\tilde{\tilde{w}}_z), \tag{34}$$

where

$$\rho_3^{\mathrm{QM}}(x_3,y_3,z_3;x_3',y_3',z_3') = \int_{-\infty}^{+\infty} \mathrm{d}x_2 \int_{-\infty}^{+\infty} \mathrm{d}x_2'\, \mathrm{e}^{\frac{\mathrm{i}k}{2L_2}((x_3-x_2)^2-(x_3'-x_2')^2)} \times \int_{-\infty}^{+\infty} \mathrm{d}y_2 \int_{-\infty}^{+\infty} \mathrm{d}y_2'\, \mathrm{e}^{\frac{\mathrm{i}k}{2L_2}((y_3-y_2)^2-(y_3'-y_2')^2)} \times \int_{-\infty}^{+\infty} \mathrm{d}z_2 \int_{-\infty}^{+\infty} \mathrm{d}z_2'\, \mathrm{e}^{\frac{\mathrm{i}k}{2L_2}((z_3-z_2)^2-(z_3'-z_2')^2)} \times \rho_2(x_2,y_2,z_2;x_2',y_2',z_2') \tag{35}$$

is the free quantum mechanical evolution of $\rho_2(x_2,y_2,z_2;x_2',y_2',z_2')$ for a time t_2.

[z_3]: We now set $x = x_3 = x_3'$, $y = y_3 = y_3'$ and $z = z_3 = z_3'$ to obtain the probability density function $p_3(x,y,z) = \rho_3(x,y,z;x,y,z)$, as the molecule interacts with the detector. However, we are only interested in the probability of detecting a particle at a horizontal coordinate x, therefore we consider:

$$p(x) = \int_{-\infty}^{+\infty} \mathrm{d}y \int_{-\infty}^{+\infty} \mathrm{d}z\, p_3(x,y,z). \tag{36}$$

It is straightforward to perform the integrations along the x axis in equation (36) at this step of the calculation. In fact, these calculations are completely analogous to those described above (equations (9) to (16)), when working within the 1D approximation.

Let us now look at the tedious integrations associated with the y axis in equation (36). In particular, we have from equation (34):

$$\int \mathrm{d}y \int \mathrm{d}y_2 \int \mathrm{d}y_2' \rho_2(x_2,y_2,z_2;x_2',y_2',z_2')\, \mathrm{e}^{\frac{\mathrm{i}k}{2L_2}(-2(y+\frac{\tilde{s}}{\tilde{w}_y})y_2+2(y+\frac{\tilde{s}}{\tilde{w}_y})y_2')}\, \mathrm{e}^{\frac{\mathrm{i}k}{2L_2}(y_2^2-y_2'^2)}. \tag{37}$$

By performing the y integration we obtain a delta function $\delta(y_2 - y_2')$ and by performing then also the y_2' integration, the expression given in equation (37) reduces to:

$$\int \mathrm{d}y_2 \rho_2(x_2,y_2,z_2;x_2',y_2,z_2'). \tag{38}$$

Let us now write the integrations associated with the y axis contained within ρ_2 (see equations (33) and (27)):

$$\int \mathrm{d}\tilde{k}_y \int \mathrm{d}\tilde{w}_y \int \mathrm{d}y_2\ \exp\left[-\frac{2\tilde{w}_y^2 + 2y_2^2 + \tilde{w}_y(4y_2 + \frac{\mathrm{i}}{\hbar}\tilde{k}_y\sigma_2^2)}{\sigma_2^2}\right] \times F(\tilde{k}_x,\tilde{k}_y,\tilde{k}_z;x_2-x_2',0,z_2-z_2';t_1). \tag{39}$$

By performing the y_2 integration we remove the quadratic term containing $\tilde{w}_y$:

$$\int \mathrm{d}\tilde{k}_y \int \mathrm{d}\tilde{w}_y\, F(\tilde{k}_x,\tilde{k}_y,\tilde{k}_z;x_2-x_2',0,z_2-z_2';t_1) \exp\left[-\frac{\mathrm{i}}{\hbar}\tilde{w}_y\tilde{k}_y\right]. \tag{40}$$

The $\tilde{w}_y$ integration yields a delta function $\delta(\tilde{k}_y)$ and by then also performing the $\tilde{k}_y$ integration, the expression given in equation (40) reduces to:

$$F(\tilde{k}_x, 0, \tilde{k}_z; x_2 - x_2', 0, z_2 - z_2'; t_1). \tag{41}$$

In addition, we have just shown that $\rho_3^{\mathrm{QM}}(x_3 + \tilde{\tilde{w}}_x, y_3 + \tilde{\tilde{w}}_y, z_3 + \tilde{\tilde{w}}_z; x_3 + \tilde{\tilde{w}}_x, y_3 + \tilde{\tilde{w}}_y, z_3 + \tilde{\tilde{w}}_z)$ defined in equation (35) does not depend on $\tilde{\tilde{w}}_y$. Hence we can perform the following integrations:

$$\int \mathrm{d}\tilde{\tilde{w}}_y \int \mathrm{d}\tilde{\tilde{k}}_y \; \mathrm{e}^{-\frac{\mathrm{i}}{\hbar}\tilde{\tilde{w}}_z\tilde{\tilde{k}}_z} F(\tilde{\tilde{k}}_x, \tilde{\tilde{k}}_y, \tilde{\tilde{k}}_z; 0, 0, 0, t_2). \tag{42}$$

Since the $\tilde{\tilde{w}}_y$ integration yields a delta function $\delta(\tilde{\tilde{k}}_y)$ we obtain from the expression given in equation (42):

$$F(\tilde{\tilde{k}}_x, 0, \tilde{\tilde{k}}_z; 0, 0, 0, t_2). \tag{43}$$

We have thus shown that the final probability density is not affected by the dynamics along the y axis. A completely analogous calculation can be performed for the integrations associated with the z axis. Hence we obtain from equation (36), relabeling x_3 as x, the interference pattern in equation (15).

This calculation thus justifies, and gives the limits of applicability, of the 1D treatment discussed before.

2.3. Far-field

The experimental setup for the far-field interference experiments is summarized in figure 3 (left). The difference with respect to the idealized situation described here above is that instead of a single point source we have an incoherent source of horizontal extension s, centred at $x_1 = 0$. We obtain the interference pattern by integrating equation (15) over the points x_1 of the source from $-\frac{s}{2}$ to $\frac{s}{2}$:

$$\begin{aligned} p(x) = &\int_{-\infty}^{+\infty} \mathrm{d}x_2 \int_{-\infty}^{+\infty} \mathrm{d}x_2' \, D(x_2 - x_2') \, \mathrm{e}^{-\frac{\mathrm{i}k}{L_2}(x_2 - x_2')x} \\ &\times \operatorname{sinc}\left(\frac{k}{2L_1}(x_2 - x_2')s\right) \mathrm{e}^{\mathrm{i}k(x_2^2 - x_2'^2)(\frac{1}{2L_1} + \frac{1}{2L_2})}. \end{aligned} \tag{44}$$

A related study of far-field decoherence effects in the Wigner function formalism is given in [41].

Let us discuss how to evaluate numerically equation (44). We recognize from the factor $\mathrm{e}^{-\frac{\mathrm{i}k}{L_2}(x_2 - x_2')x_3}$ a Fourier transform and an inverse Fourier transform. Fourier transforms can be approximated with discrete Fourier transforms using the FFT algorithm. Hence the integrations in equation (44) can be conveniently evaluated numerically with the row column FFT algorithm.

2.4. Talbot–Lau near-field

The experimental setup for the KDTL near-field interference experiment is represented in figure 3(right). This is essentially the same scheme as presented before (figure 1) except that now we have two additional gratings at positions z_1, z_3 along the optical axis. We assume that all gratings have a very large horizontal extension such that we can model them by periodic functions. The first grating at z_1 acts as a mask of an infinite incoherent source and similarly

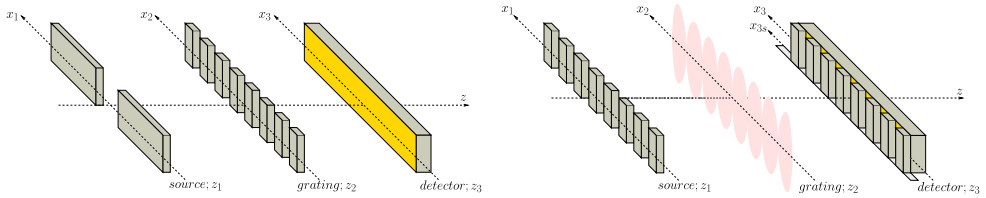

Figure 3. Left: far-field experimental setup. The optical elements are: an incoherent source at z_1 (centered on the optical axis, i.e. around $x_1 = 0$), the diffraction grating at z_2 (here we have shown a mechanical grating with $N = 7$ slits) and the detector at z_3. For the experiment described in section 5 we have the following numerical values. The distance from z_1 to z_2 is $L_1 = 0.702$ m and the distance from z_2 to z_3 is $L_2 = 0.564$ m. The source extension is taken to be $s = 1\mu$m. The mechanical grating with $N = 30$ slits is described by the period $d = 100$ nm and slit width $l = 79$ nm. The van der Walls forces due to the grating are modelled by an effective slit width $l_{\text{eff}} = 43$ nm. Right: Talbot–Lau near-field experimental setup. In this case the optical elements are: an extended incoherent source at z_1, a diffraction grating at z_2 (here, an optical grating produced by a standing light wave) and the detector at z_3. Two additional mechanical gratings block part of the molecules: the mechanical grating located immediately after the source is held fixed, while the mechanical grating immediately before the detector can move along the x_3 axis (we denote the displacement from its initial position by x_{3s}). We assume that all elements have a very large horizontal extension such that one can approximate them with periodic functions. The detector at z_3 records molecules that arrive at all points along the x_3 axis in a certain amount of time. For the experiment described in section 5 we have the following numerical values. The distance from z_1 to z_2 and the distance from z_2 to z_3 is $L = L_1 = L_2 = 10.5$ cm. Both mechanical gratings are described by the same period $d = 266$ nm and slit width $l = 110$ nm. The optical grating is described by the wavelength $\lambda_{\text{laser}} = 532$ nm, the laser power $P_{\text{laser}} = 1$ W, the optical polarizability $\alpha_{\text{opt}} = 410$ Å $\times\, 4\pi\epsilon_0$ and the absorption cross section $\sigma_a = 1.7 \times 10^{-21}$ m^2.

the third grating at z_3 acts as a mask of the infinite detection screen. The experiment is performed by moving the masking grating at z_3 along the x_3 axis and recording the total number of molecules that reach the detector in a given amount of time. At the end one obtains the number of molecules that reach the detector given a given displacement x_{3s} of the third grating from its initial position.

In section 5 we will describe the KDTL experiment, where the 3 gratings have the same periodicity d and the distance from z_1 to z_2 and from z_2 to z_3 is $L = L_1 = L_2$. Due to the periodicity of the 3 gratings, we adopt the following notation for the Fourier series of the corresponding transmission functions (notation of [42]):

$$|t_1(x_1)|^2 = \sum_{l=-\infty}^{+\infty} A_l \, \mathrm{e}^{\mathrm{i}2\pi l \frac{x_1}{d}}, \tag{45}$$

$$t(x_2) = \sum_{j=-\infty}^{+\infty} b_j \, \mathrm{e}^{\mathrm{i}2\pi j \frac{x_2}{d}}, \tag{46}$$

$$|t_3(x_3)|^2 = \sum_{n=-\infty}^{+\infty} C_n \, \mathrm{e}^{\mathrm{i}2\pi n \frac{x_3}{d}}. \tag{47}$$

We can now directly proceed with the derivation of the interference pattern starting again from equation (15):

$$S(x_{3s}) = \int_{-\infty}^{+\infty} \mathrm{d}x_1 \int_{-\infty}^{+\infty} \mathrm{d}x_3\, p(x_3;x_1)|t_1(x_1)|^2|t_3(x_3-x_{3s})|^2, \tag{48}$$

where with respect to the far-field experiment, there is a further integration over all the detector region, x_{3s} is the horizontal shift of the third grating and $p(x_3;x_1)$ is the interference pattern due to a single source point at x_1 given by equation (15). In other words, $S(x_{3s})$ gives the number of molecules that reach the infinite detector at z_3 from the infinite source at z_1 in a given amount of time, given a displacement x_{3s} of the third grating from its initial position. Since this gives formally an infinite value, we have to properly normalize the result. This is done in the following way.

The integrations in equation (48) over x_1, x_3 yield two delta functions $\delta(\frac{2\pi l}{d} - \frac{k}{L_1}(x_2 - x_2'))$, $\delta(\frac{2\pi n}{d} - \frac{k}{L_2}(x_2 - x_2'))$. We perform the integration over $\mathrm{d}x_2'$ which gives the constraint $x_2 - x_2' = \frac{2\pi l}{d}\frac{L}{k}$, while the other delta function gives the constrain $l = n$. We now divide by $\delta(0)$ in order to remove the infinite factor due to the delta function giving this first constrain. We are left with the integration over $\mathrm{d}x_2$ which gives a delta function $\delta(\frac{4\pi n}{d} + \frac{2\pi j}{d} - \frac{2\pi j'}{d})$, where j' is the index in the Fourier expansion of $t^*(x_2')$. This gives the constraint $j' = j + 2n$. We again divide by $\delta(0)$ in order to remove the infinite factor due to the delta function giving this second constrain. We are now left with a finite expression. In order to obtain a notation consistent with that of [42] we relabel n as $-n$ and use the fact that $A_{-n} = A_n^*$, $C_{-n} = C_n^*$. Thus we obtain:

$$S(x_{3s}) = \sum_n A_n^* C_n^* B_n D \left(\frac{2\pi n}{d}\frac{L}{k}\right) \mathrm{e}^{\mathrm{i}2\pi n \frac{x_{3s}}{d}}, \tag{49}$$

where $B_n = \sum_j b_j b_{j-n}^* \mathrm{e}^{\mathrm{i}\frac{\pi^2}{d^2}\frac{L}{k}(n^2-2nj)}$. The above equation coincides with the results derived by using the Wigner function formalism [38, 40].

3. Summary of collapse models and of the interference pattern

3.1. CSL: continuous spontaneous localization

Here we are referring to the mass-proportional version of the CSL model [43]. The single-particle master equation in 3D is given by [44]:

$$\frac{\mathrm{d}}{\mathrm{d}t}\hat{\rho}(t) = -\frac{\mathrm{i}}{\hbar}\left[\hat{H},\hat{\rho}(t)\right] + \lambda\frac{m^2}{m_0^2}\left(\left(\frac{r_C}{\sqrt{\pi}\hbar}\right)^3 \int \mathrm{d}^3\boldsymbol{Q}\, \mathrm{e}^{-\frac{\boldsymbol{Q}^2 r_C^2}{\hbar^2}}\, \mathrm{e}^{\frac{\mathrm{i}}{\hbar}\boldsymbol{Q}\cdot\hat{\boldsymbol{x}}}\hat{\rho}(t)\, \mathrm{e}^{-\frac{\mathrm{i}}{\hbar}\boldsymbol{Q}\cdot\hat{\boldsymbol{x}}} - \hat{\rho}(t)\right). \tag{50}$$

The physical meaning of the phenomenological constants λ and r_C was clarified in section 1. In the free-particle case $\hat{H} = \hat{p}^2/2m$, the equation can be solved exactly. In the coordinate basis, it reads [12]:

$$\rho^{\mathrm{CSL}}(\boldsymbol{x},\boldsymbol{x}',t) = \frac{1}{(2\pi\hbar)^3}\int \mathrm{d}\tilde{\boldsymbol{k}} \int \mathrm{d}\tilde{\boldsymbol{w}}\ \mathrm{e}^{-\frac{\mathrm{i}}{\hbar}\tilde{\boldsymbol{k}}\cdot\tilde{\boldsymbol{w}}} F_{\mathrm{CSL}}(\tilde{\boldsymbol{k}},\boldsymbol{x}-\boldsymbol{x}',t)\rho^{\mathrm{QM}}(\boldsymbol{x}+\tilde{\boldsymbol{w}},\boldsymbol{x}'+\tilde{\boldsymbol{w}},t), \tag{51}$$

where $\rho^{\mathrm{QM}}(\boldsymbol{x},\boldsymbol{x}',t)$ is the standard free quantum evolution for the density matrix ($\lambda = 0$) and

$$F_{\mathrm{CSL}}(\tilde{\boldsymbol{k}},\boldsymbol{q},t) = \exp\left[-\lambda\frac{m^2}{m_0^2}t\left(1 - \frac{1}{t}\int_0^t \mathrm{d}\tau\ \mathrm{e}^{-\frac{1}{4r_C^2}(\boldsymbol{q}-\frac{\tilde{\boldsymbol{k}}\tau}{m})^2}\right)\right]. \tag{52}$$

The interference pattern is given by equation (15) with the function D defined as follows:

$$D_{\mathrm{CSL}}(x_2 - x_2') = \exp\left[-\lambda \frac{m^2}{m_0^2}(t_1 + t_2)\left(1 - \frac{\sqrt{\pi}\,\mathrm{erf}(\frac{(x_2 - x_2')}{2r_C})}{\frac{(x_2 - x_2')}{2r_C}}\right)\right]. \tag{53}$$

Note that $D_{\mathrm{CSL}}(x_2 - x_2')$ was previuosly derived [38, 40, 41] by using the Wigner function's formalism.

The GRW single-particle master equation has the same mathematical structure as the CSL single-particle master equation. Since our analysis is based entirely on this master equation the above CSL formulae apply also to the GRW model, the only difference being the amplification mechanism discussed before.

3.2. DP: Diósi-Penrose

The single-particle master equation in 3D for a particle of mass m_0 is given by [13, 24]:

$$\frac{\mathrm{d}\hat{\rho}_t}{\mathrm{d}t} = -\frac{\mathrm{i}}{\hbar}\left[\hat{H}, \hat{\rho}_t\right] + \frac{Gm_0^2}{2\pi\hbar^2}\int \mathrm{d}\boldsymbol{Q}\frac{1}{\boldsymbol{Q}^2}\,\mathrm{e}^{-\frac{\boldsymbol{Q}^2 R_0^2}{\hbar^2}}\left(\mathrm{e}^{\frac{\mathrm{i}}{\hbar}\boldsymbol{Q}\cdot\hat{x}}\hat{\rho}_t\,\mathrm{e}^{-\frac{\mathrm{i}}{\hbar}\boldsymbol{Q}\cdot\hat{x}} - \hat{\rho}_t\right), \tag{54}$$

where R_0 is a regularization parameter, which has to be included in order to avoid divergences at short distances. Loosely speaking, the effective collapse rate, analogous to λ, is given by $Gm_0^2/\sqrt{\pi}\hbar R_0$, while R_0 describes how well an object is localized, analogous to r_C. For a point-like particle of mass m we have to replace m_0 with m. In the free-particle case, the equation can be solved exactly, and in the position representation it reads [24]:

$$\rho^{\mathrm{DP}}(\boldsymbol{x}, \boldsymbol{x}', t) = \frac{1}{(2\pi\hbar)^3}\int \mathrm{d}\tilde{\boldsymbol{k}}\int \mathrm{d}\tilde{\boldsymbol{w}}\;\mathrm{e}^{-\frac{\mathrm{i}}{\hbar}\tilde{\boldsymbol{k}}\cdot\tilde{\boldsymbol{w}}}F_{\mathrm{DP}}(\tilde{\boldsymbol{k}}, \boldsymbol{x} - \boldsymbol{x}', t)\rho^{\mathrm{QM}}(\boldsymbol{x} + \boldsymbol{w}, \boldsymbol{x}' + \boldsymbol{w}, t), \tag{55}$$

where, again, $\rho^{\mathrm{QM}}(\boldsymbol{x}, \boldsymbol{x}', t)$ is the free standard quantum evolution, and

$$F_{\mathrm{DP}}(\tilde{\boldsymbol{k}}, \boldsymbol{q}, t) = \exp\left[-\frac{1}{\hbar}\int_0^t \mathrm{d}\tau\left(U(-\frac{\tilde{\boldsymbol{k}}\tau}{m} + \boldsymbol{q}) - U(0)\right)\right] \tag{56}$$

with $U(\boldsymbol{x}) = -Gm_0^2\,\mathrm{erf}(|\boldsymbol{x}|/2R_0)/|\boldsymbol{x}|$.

The interference pattern is given again by equation (15), with the function D given by:

$$D_{\mathrm{DP}}(x_2 - x_2') = \exp\left[-\frac{Gm_0^2}{\hbar\sqrt{\pi}R_0}(t_1 + t_2)\left(1 - {}_2F_2\left(\frac{1}{2}, \frac{1}{2}, \frac{3}{2}, \frac{3}{2}; -\left(\frac{|x_2 - x_2'|}{2R_0}\right)^2\right)\right)\right], \tag{57}$$

where ${}_2F_2(\frac{1}{2}, \frac{1}{2}, \frac{3}{2}, \frac{3}{2}; z) = \sum_{k=0}^{\infty}\left(\frac{1}{1+2k}\right)^2\frac{z^k}{k!}$.

It is instructive to compare D_{DP} and D_{CSL}. One can relate the role of λ in the CSL model with $\lambda_{\mathrm{DP}} = \frac{Gm_0^2}{\hbar\sqrt{\pi}R_0}$ in the DP model, and the role of r_C for CSL with R_0 for DP. As figure 4 shows, when appropriately rescaled, D_{DP} and D_{CSL} have a very similar behaviour. In particular, both are equal to 1 for $|x_2 - x_2'| = 0$ and decay more or less in the same way towards the asymptotic value $\mathrm{e}^{-\lambda(t_1+t_2)}$ as $|x_2 - x_2'| \to \infty$.

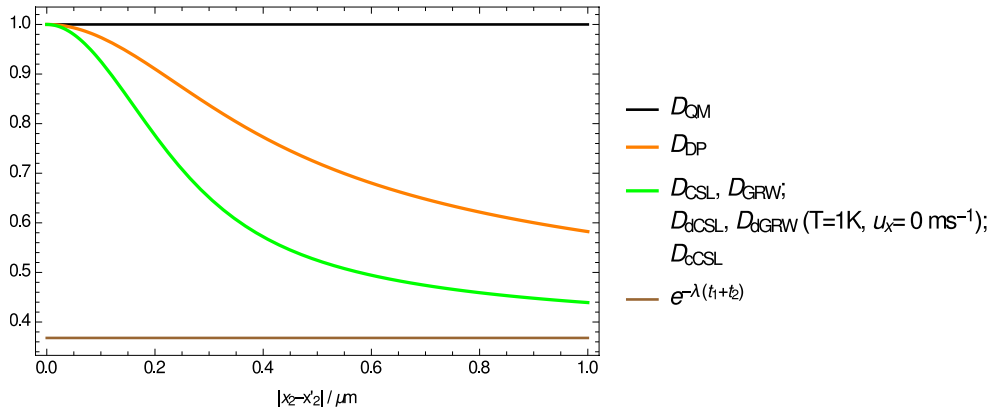

Figure 4. Comparison of D functions for the considered collapse models. The plot is obtained with $r_C = 10^{-7}$ m, $\lambda = 500\ \ \mathrm{s}^{-1}$, $t_1 = t_2 = 1$ ms, $L_1 = L_2 = 0.1$ m, $R_0 = 10^{-7}$ m, $\lambda_{\mathrm{DP}} = \lambda = 500\ \ \mathrm{s}^{-1}$, where the rescaled λ, λ_{DP} are such that $\lambda(t_1 + t_2) = 1$. The black solid line represents the quantum mechanical function ($D = 1$), the orange solid line represents the D function for the DP model, the green solid line represents that of the CSL, GRW, dCSL, dGRW and cCSL models (for temperatures $T > 10^{-7}$ K and boost along the x axis $u_x < 10^4\ \mathrm{ms}^{-1}$. The solid brown line represents the asymptotic value of the D functions for all the considered collapse models as $|x - x'| \to +\infty$.

3.3. dCSL: dissipative CSL

This is a recently developed new version of the CSL model, which includes dissipative effects, which prevent the energy of the system to increase and eventually diverge. The single-particle master equation in 3D is [15, 24]:

$$\frac{\mathrm{d}\hat{\rho}_t}{\mathrm{d}t} = -\frac{\mathrm{i}}{\hbar}\left[\hat{H}, \hat{\rho}_t\right] + \lambda\frac{m^2}{m_0^2}\left(\left(\frac{r_C(1+k_T)}{\sqrt{\pi}\hbar}\right)^3 \int \mathrm{d}\boldsymbol{Q}\, \mathrm{e}^{\frac{\mathrm{i}}{\hbar}\boldsymbol{Q}\cdot\hat{\boldsymbol{x}}}\, \mathrm{e}^{-\frac{r_C^2}{2\hbar^2}((1+k_T)\boldsymbol{Q}+2k_T\hat{\boldsymbol{p}})^2}\, \hat{\rho}_t\, \mathrm{e}^{-\frac{r_C^2}{2\hbar^2}((1+k_T)\boldsymbol{Q}+2k_T\hat{\boldsymbol{p}})^2}\, \mathrm{e}^{-\frac{\mathrm{i}}{\hbar}\boldsymbol{Q}\cdot\hat{\boldsymbol{x}}} - \hat{\rho}\right) \tag{58}$$

where $k_T = \frac{\hbar^2}{8mr_C^2k_{\mathrm{B}}T}$, k_{B} is the Boltzmann constant and T the temperature the system thermalizes to. This is a new parameter of the theory, which together with λ and r_C fully identifies the model. In the limit $k_T \to 0$ (i.e. $T \to \infty$), one re-obtains standard CSL model.

We simplify the analysis, as in [15, 24], by considering only small values of k_T:

$$k_T \ll 1. \tag{59}$$

This assumption identifies a region in the parameter space (T,r_C), depicted in figure 5.

In the free particle case the solution reads [15]:

$$\rho^{\mathrm{dCSL}}(\boldsymbol{x},\boldsymbol{x}',t) = \frac{1}{(2\pi\hbar)^3}\int \mathrm{d}\tilde{\boldsymbol{k}} \int \mathrm{d}\tilde{\boldsymbol{w}}\ \mathrm{e}^{-\frac{\mathrm{i}}{\hbar}\tilde{\boldsymbol{k}}\cdot\tilde{\boldsymbol{w}}} F_{\mathrm{dCSL}}(\tilde{\boldsymbol{k}},\boldsymbol{x}-\boldsymbol{x}',t)\rho^{\mathrm{QM}}(\boldsymbol{x}+\tilde{\boldsymbol{w}},\boldsymbol{x}'+\tilde{\boldsymbol{w}},t), \tag{60}$$

where as usual $\rho^{\mathrm{QM}}(\boldsymbol{x},\boldsymbol{x}',t)$ is the free standard quantum evolution, and

$$F_{\mathrm{dCSL}}(\tilde{\boldsymbol{k}},\boldsymbol{q},t) = \exp\left[-\lambda\frac{m^2}{m_0^2}t\left(1 - \frac{1}{t}\int_0^t \mathrm{d}\tau\ \mathrm{e}^{-\frac{\tilde{k}^2r_C^2k_T^2}{\hbar^2} - \frac{(-\frac{\tilde{k}\tau}{m}+q)^2}{4r_C^2(1+k_T)^2}}\right)\right]. \tag{61}$$

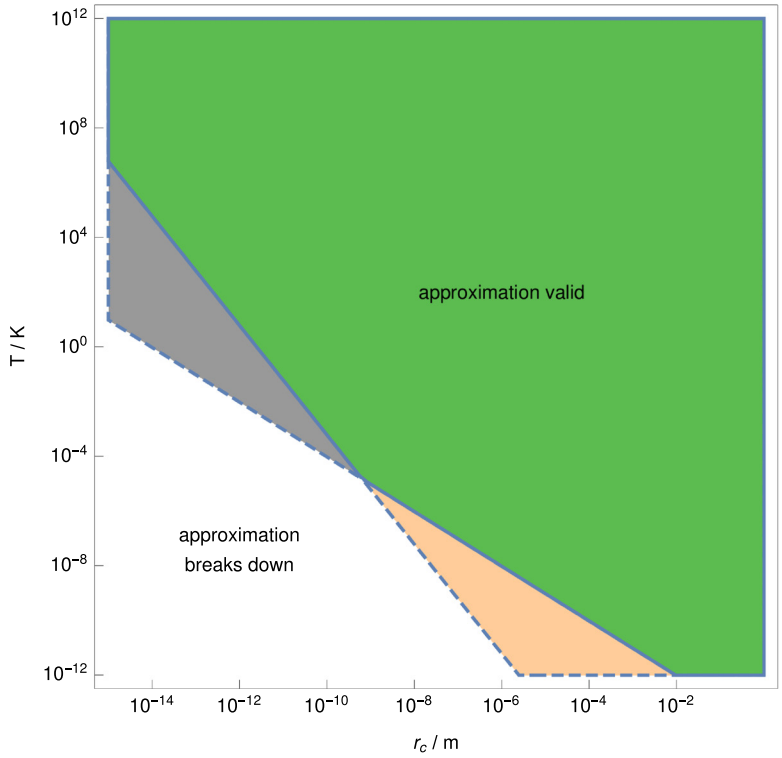

Figure 5. Graphical depiction of the conditions given in equations (59) and (63). The condition given by equation (59) is satisfied in the orange and green regions, while the condition given in equation (63) is satisfied in the gray and green regions: both conditions are satisfied in the green region. We estimate these limits for experimental situations, where the spatial and temporal extension of the superpositions is limited to distances $\Delta x < 10^{-5}$ m and duration $t < 10^{-2}$ s, respectively. Reprinted from [39], Copyright (2017), with permission from Elsevier.

The interference pattern is still given by equation (15), with the function D given by:

$$D_{\mathrm{dCSL}}(x_2 - x_2') = \exp\Big[-\lambda \frac{m^2}{m_0^2}(t_1 + t_2) + \lambda \frac{m^2}{m_0^2}\left(t_1\, \mathrm{e}^{-\frac{k^2}{L_1^2}(x_2-x_2')^2 r_C^2 k_T^2} + t_2\, \mathrm{e}^{-\frac{k^2}{L_2^2}(x_2-x_2')^2 r_C^2 k_T^2} \right) \frac{\sqrt{\pi}}{2} \frac{\mathrm{erf}\left(\frac{(x_2-x_2')}{2r_C(1+k_T)}\right)}{\frac{(x_2-x_2')}{2r_C(1+k_T)}} \Big]. \tag{62}$$

We note that this equation reduces to the CSL D-function, given in equation (53), when the following condition is fulfilled:

$$r_C t \gg \frac{\hbar \Delta x}{8 k_B T}, \tag{63}$$

for $t = t_1$ and $t = t_2$. We estimate these limits for experimental situations, where the spatial and temporal extension of the superpositions is limited to distances $\Delta x < 10^{-5}$ m and duration $t < 10^{-2}$ s, respectively. This condition identifies a region in the parameter space (r_C,T), depicted in figure 5.

However, the master equation (58) is not invariant under boosts. Indeed, the dissipative CSL master equation has the same structure of a quantum linear Boltzmann equation of a particle immersed in a finite temperature bath [23]. Thus the dissipative CSL model contains an additional free parameter, a velocity $\boldsymbol{u}$, which is analogous to the relative velocity between bath and particle. In particular, the master equation in the boosted reference frame with boost velocity $\boldsymbol{u}$ is given by the following equation:

$$\frac{\mathrm{d}\hat{\rho}_t}{\mathrm{d}t} = -\frac{\mathrm{i}}{\hbar}\left[\hat{H},\hat{\rho}_t\right] + \lambda\frac{m^2}{m_0^2}\Big(\left(\frac{r_C(1+k_T)}{\sqrt{\pi}\hbar}\right)^3 \times \int \mathrm{d}\boldsymbol{Q}\, \mathrm{e}^{\frac{\mathrm{i}}{\hbar}\boldsymbol{Q}\cdot\hat{\boldsymbol{x}}}\, \mathrm{e}^{-\frac{r_C^2}{2\hbar^2}((1+k_T)\boldsymbol{Q}+2k_T(\hat{\boldsymbol{p}}-m\boldsymbol{u}))^2}\hat{\rho}_t\, \mathrm{e}^{-\frac{r_C^2}{2\hbar^2}((1+k_T)\boldsymbol{Q}+2k_T(\hat{\boldsymbol{p}}-m\boldsymbol{u}))^2}\, \mathrm{e}^{-\frac{\mathrm{i}}{\hbar}\boldsymbol{Q}\cdot\hat{\boldsymbol{x}}} - \hat{\rho}\Big)\,. \tag{64}$$

We find the solution of equation (64) using the characteristic function approach [45]. The solution is given by equation (60) with the function F_{dCSL} replaced by:

$$F_{\mathrm{dCSL}}^{\mathrm{boosted}}(\tilde{\boldsymbol{k}},\boldsymbol{q},t;\boldsymbol{u}) = \exp\left[-\lambda\frac{m^2}{m_0^2}t\left(1-\frac{1}{t}\int_0^t \mathrm{d}\tau\, \mathrm{e}^{-\frac{\tilde{\boldsymbol{k}}^2 r_C^2 k_T^2}{\hbar^2}-\frac{(-\frac{\tilde{\boldsymbol{k}}\tau}{m}+\boldsymbol{q})^2}{4r_C^2(1+k_T)^2}}\, \mathrm{e}^{\frac{\mathrm{i}}{\hbar}\frac{2k_T m\boldsymbol{u}}{1+k_T}\cdot(-\frac{\tilde{\boldsymbol{k}}\tau}{m}+\boldsymbol{q})}\right)\right]. \tag{65}$$

The interference pattern is given by equation (15) with the function D replaced by:

$$\begin{aligned} D_{\mathrm{dCSL}}^{\mathrm{boosted}}(x_2-x_2') = \exp\Big[&-\lambda\frac{m^2}{m_0^2}(t_1+t_2) \\ &+\lambda\frac{m^2}{m_0^2}\left(t_1\, \mathrm{e}^{-\frac{k^2}{L_1^2}(x_2-x_2')^2 r_C^2 k_T^2} + t_2\, \mathrm{e}^{-\frac{k^2}{L_2^2}(x_2-x_2')^2 r_C^2 k_T^2}\right) \\ &\times \frac{\int_0^{(\frac{(x_2-x_2')}{2r_C(1+k_T)})}\mathrm{d}\tau\, \mathrm{e}^{-\tau^2}\cos(2\tau\frac{2r_C k_T m u_x}{\hbar})}{(\frac{(x_2-x_2')}{2r_C(1+k_T)})}\Big], \end{aligned} \tag{66}$$

where u_x is the x component of $\boldsymbol{u}$. We note that this equation reduces to the CSL D-function, given in equation (53), when in addition to equation (63), the following condition is fulfilled:

$$\frac{r_C^2}{u_x} \gg \frac{\hbar\Delta x}{8k_{\mathrm{B}}T}. \tag{67}$$

We note that equation (66) reduces to equation (62) as $u_x \to 0$ and that equation (62) reduces to equation (53) as $k_T \to 0$. We estimate these limits for experimental situations, where the spatial and temporal extension of the superpositions is limited to distances $\Delta x < 10^{-5}$ m and duration $t < 10^{-2}$ s, respectively. This condition identifies a region in the parameter space (r_C, u_x, T), depicted in figure 6.

A comparison of $D_{\mathrm{dCSL}}^{\mathrm{boosted}}$ functions evaluated with different temperatures T and different boosts u_x is given in figures 7 and 8 respectively. We see from these figures that the dCSL model with large temperatures T and small boosts u_x give the smallest modification with respect to the standard quantum mechanical evolution ($D = 1$) and practically coincide with the CSL model evolution. Hence, given that T and u_x are unknown, the CSL model can be used as a bound for all dCSL models with arbitrary T and $\boldsymbol{u}$.

The dGRW single-particle master equation has the same mathematical structure as the dCSL single-particle master equation. Since our analysis is based entirely on this master equation the above dCSL formulae apply also to the dGRW model, the only difference being the amplification mechanism discussed in section 4.

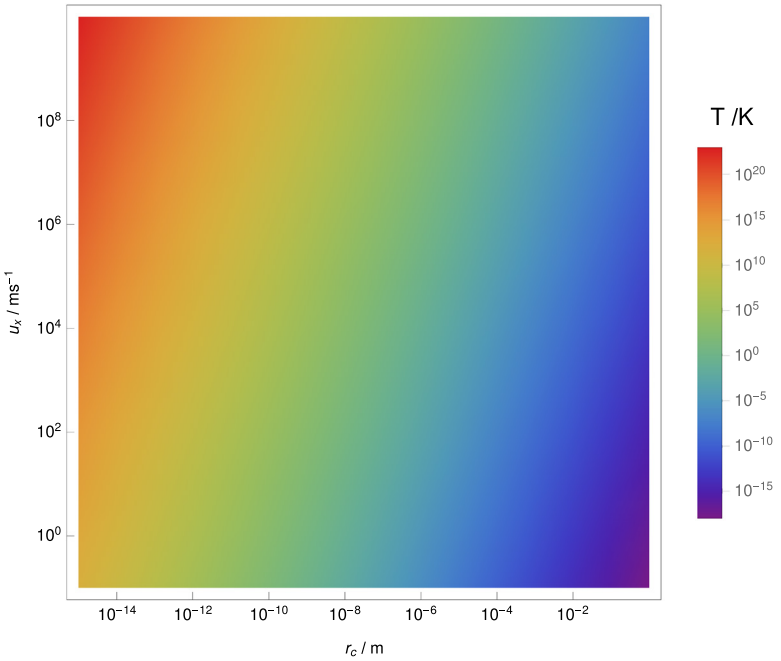

Figure 6. Graphical depiction of the condition given in equation (67). The color indicates the minimum temperature, for a given value of r_C and u_x, such that the condition given in equation (67) is satisfied. We estimate these limits for experimental situations, where the spatial and temporal extension of the superpositions is limited to distances $\Delta x < 10^{-5}$ m and duration $t < 10^{-2}$ s, respectively. Reprinted from [39], Copyright (2017), with permission from Elsevier.

3.4. cCSL: colored CSL

This model presents an additional difficulty with respect to the white noise models discussed here above. The previous calculation splits into two parts, the free evolution from the source at time τ_1 to the grating at time τ_2 and the free evolution from the grating at time τ_2 to the detector at time τ_3, whereas at time τ_2 the molecule is subject to a non free evolution. Let us consider the times $\tau_1 < t_{\text{before}} < \tau_2$ and $\tau_2 < t_{\text{after}} < \tau_3$. The non white noise might correlate the evolution between t_{before} and t_{after}. In order to simplify the analysis we neglect the correlations between these times by assuming a small correlation time $\tau_C \ll \tau_3 - \tau_1$. A similar argument can be put forward for the correlation between times before and after τ_1. Hence we limit the discussion to non white CSL models with small correlation times. In particular, this assumption justifies the following approximation of the free one particle master equation in 3D [18, 46]:

$$\frac{\mathrm{d}\hat{\rho}_t}{\mathrm{d}t} = -\frac{\mathrm{i}}{\hbar}\left[\hat{H},\hat{\rho}_t\right] - \lambda\frac{m^2}{m_0^2}\left(\frac{r_C}{\sqrt{\pi}\hbar}\right)^3\int_0^t \mathrm{d}s f(t-s)\int \mathrm{d}\boldsymbol{Q}\,\mathrm{e}^{-\frac{\boldsymbol{Q}^2 r_C^2}{\hbar^2}}\left[\,\mathrm{e}^{\frac{\mathrm{i}}{\hbar}\hat{\boldsymbol{x}}\cdot\boldsymbol{Q}},\left[\hat{U}^\dagger(s-t)\,\mathrm{e}^{-\frac{\mathrm{i}}{\hbar}\hat{\boldsymbol{x}}\cdot\boldsymbol{Q}}\hat{U}(s-t),\hat{\rho}_t\right]\right], \tag{68}$$

where $f(t-s)$ is the correlation function and $\hat{U}(t) = \mathrm{e}^{-\frac{\mathrm{i}}{\hbar}\frac{\hat{\boldsymbol{p}}^2}{2m}t}$.

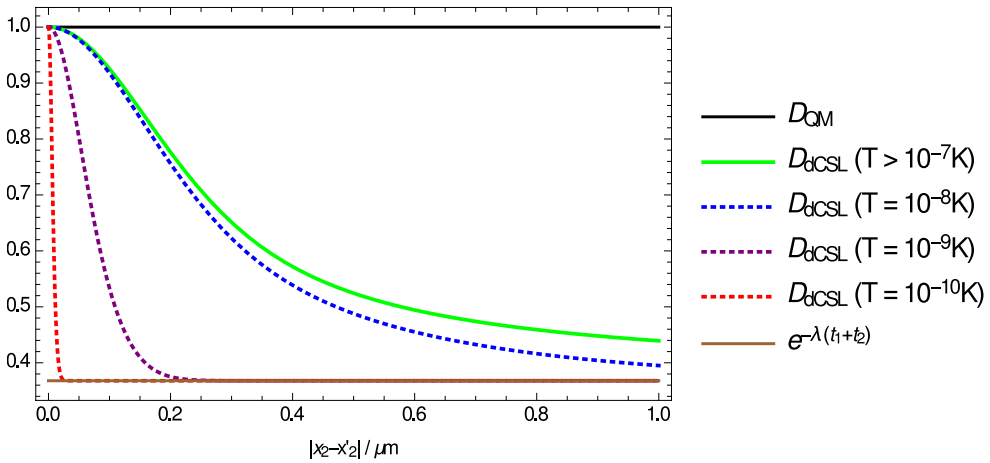

Figure 7. Comparison of D_{dCSL} functions for different temperatures T at fixed boost $u_x = 0$. The plot is obtained with $r_C = 10^{-7}$ m, $\lambda = 500$ s^{-1}, $t_1 = t_2 = 1$ ms and $L_1 = L_2 = 0.1$ m. The black solid line represents the quantum mechanical function ($D = 1$), the green solid line represents the D function for the dCSL models with $T > 10^{-7}$ K (which includes the CSL model), while the dashed lines represent the dCSL models with temperatures $T = 10^{-8}$ K, $T = 10^{-9}$ K and $T = 10^{-10}$ K. The solid brown line represents the asymptotic value of the D functions for all the considered collapse models as $|x - x'| \to +\infty$. Reprinted from [39], Copyright (2017), with permission from Elsevier.

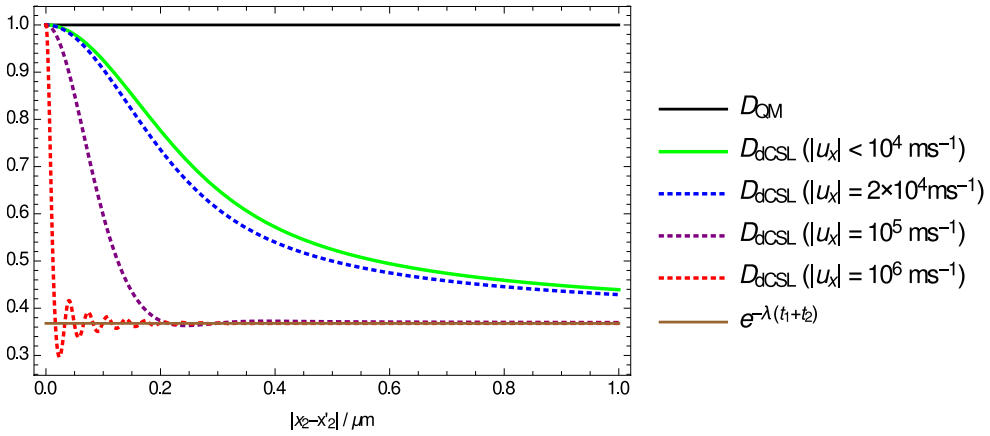

Figure 8. Comparison of D_{dCSL} functions for different boost along the x axis u_x at fixed temperature $T = 1K$. The plot is obtained with $r_C = 10^{-7}$ m, $\lambda = 500$ s^{-1}, $t_1 = t_2 = 1$ ms and $L_1 = L_2 = 0.1$ m. The black solid line represents the quantum mechanical function ($D = 1$), the green solid line represents the D function for the dCSL models with boosts along the x axis $|u_x| < 10^4$ ms^{-1} (which includes the CSL model), while the dashed lines represent the dCSL models with boost along the x axis $|u_x| = 2 \times 10^4$ ms^{-1}, $|u_x| = 10^5$ ms^{-1} and $|u_x| = 10^6$ ms^{-1}. The solid brown line represents the asymptotic value of the D functions for all the considered collapse models as $|x - x'| \to +\infty$.

We now expand $\hat{U}(\tau)$ to first order: $\hat{U}(\tau) \approx 1 - \frac{\mathrm{i}}{\hbar}\frac{\hat{\boldsymbol{p}}^2}{2m}\tau$, which is justified since τ is limited by the correlation time τ_C of the correlation function $f(s)$ through the time integral in equation (68). We make the following assumption:

$$\frac{1}{\hbar}\frac{\hat{\boldsymbol{p}}^2}{2m}\tau_C \ll 1. \tag{69}$$

We can make a rough estimate for the maximum value of τ_C by replacing the operator with the expectation value in equation (69): $\langle\hat{\boldsymbol{p}}^2/2m\rangle\tau_C/\hbar \ll 1$, We consider the temperature of the system to be $T \approx 10^2 - 10^3 K$. Thus based on the equipartition theorem we replace $\langle\hat{\boldsymbol{p}}^2/2m\rangle$ by $k_B T$ which gives the condition $\tau_C < 10^{-13} s$. This gives us a corresponding minimum ultraviolet frequency cut-off $\Omega \gg 10^4$ GHz for the Fourier transform of the correlation function.

Hence by performing the time integration we obtain from equation (68):

$$\frac{\mathrm{d}\hat{\rho}_t}{\mathrm{d}t} = L_{\mathrm{CSL}}[\hat{\rho}] + L_{\mathrm{correction}}[\hat{\rho}], \tag{70}$$

where

$$L_{\mathrm{CSL}}[\hat{\rho}] = -\frac{\mathrm{i}}{\hbar}\left[\hat{H},\hat{\rho}_t\right] + \lambda\frac{m^2}{m_0^2}\left(\left(\frac{r_C}{\sqrt{\pi}\hbar}\right)^3\int \mathrm{d}\boldsymbol{Q}\,\mathrm{e}^{-\frac{\boldsymbol{Q}^2 r_C^2}{\hbar^2}}\,\mathrm{e}^{\frac{\mathrm{i}}{\hbar}\boldsymbol{Q}\cdot\hat{\boldsymbol{x}}}\hat{\rho}(t)\,\mathrm{e}^{-\frac{\mathrm{i}}{\hbar}\boldsymbol{Q}\cdot\hat{\boldsymbol{x}}} - \hat{\rho}(t)\right) \tag{71}$$

is the white noise CSL evolution,

$$L_{\mathrm{correction}}[\hat{\rho}] = \frac{\mathrm{i}\bar{\tau}}{2m\hbar}\lambda\frac{m^2}{m_0^2}\left(\frac{r_C}{\sqrt{\pi}\hbar}\right)^3\int \mathrm{d}\boldsymbol{Q}\,\mathrm{e}^{-\frac{\boldsymbol{Q}^2 r_C^2}{\hbar^2}}\boldsymbol{Q}\cdot\left(\left[\,\mathrm{e}^{\frac{\mathrm{i}}{\hbar}\boldsymbol{Q}\cdot\hat{\boldsymbol{x}}}\hat{\rho}\,\mathrm{e}^{-\frac{\mathrm{i}}{\hbar}\boldsymbol{Q}\cdot\hat{\boldsymbol{x}}},\hat{\boldsymbol{p}}\right] + \mathrm{e}^{\frac{\mathrm{i}}{\hbar}\boldsymbol{Q}\cdot\hat{\boldsymbol{x}}}[\hat{\rho},\hat{\boldsymbol{p}}]\,\mathrm{e}^{-\frac{\mathrm{i}}{\hbar}\boldsymbol{Q}\cdot\hat{\boldsymbol{x}}}\right) \tag{72}$$

is the first order correction due to the non white noise and

$$\bar{\tau} = \int_0^t f(s)s\mathrm{d}s. \tag{73}$$

By performing a direct but tedious calculation, it can be shown that equation (70) is invariant under boost and thus fully Galilean invariant.

Let us now find the solution of equation (70) by using the characteristic function approach [45]. We multiply equation (70) by $\mathrm{e}^{\frac{\mathrm{i}}{\hbar}(\boldsymbol{\nu}\cdot\hat{\boldsymbol{x}}+\boldsymbol{\mu}\cdot\hat{\boldsymbol{p}})}$ and take the trace:

$$\frac{\partial}{\partial t}\chi(\boldsymbol{\nu},\boldsymbol{\mu},t) = \frac{\boldsymbol{\nu}}{M}\cdot\partial_{\boldsymbol{\mu}}\chi(\boldsymbol{\nu},\boldsymbol{\mu},t) + \lambda\left(\Phi(\boldsymbol{\nu},\boldsymbol{\mu}) - 1\right), \tag{74}$$

where

$$\Phi(\boldsymbol{\nu},\boldsymbol{\mu}) = \mathrm{e}^{\frac{-\mu^2}{4r_C^2}}\left(1 - \frac{\boldsymbol{\mu}\cdot\boldsymbol{\nu}}{4mr_C^2}\bar{\tau}\right) \tag{75}$$

and

$$\chi(\boldsymbol{\nu},\boldsymbol{\mu},t) = \mathrm{Tr}[\hat{\rho}_t\,\mathrm{e}^{\frac{\mathrm{i}}{\hbar}(\boldsymbol{\nu}\cdot\hat{\boldsymbol{x}}+\boldsymbol{\mu}\cdot\hat{\boldsymbol{p}}}]. \tag{76}$$

The solution of the characteristic function in equation (74) is given by:

$$\chi(\boldsymbol{\nu},\boldsymbol{\mu},t) = \chi^0(\boldsymbol{\nu},\boldsymbol{\mu},t)\,\mathrm{e}^{-\lambda t + \int_0^t \Phi(\boldsymbol{\nu},\frac{\boldsymbol{\nu}\tau}{m}+\boldsymbol{\mu})\mathrm{d}\tau}, \tag{77}$$

where $\chi^0(\boldsymbol{\nu},\boldsymbol{\mu},t)$ is the solution of equation $\frac{\partial}{\partial t}\chi^0(\boldsymbol{\nu},\boldsymbol{\mu},t) = \frac{1}{m}\boldsymbol{\nu}\cdot\frac{\partial}{\partial\boldsymbol{\mu}}\chi^0(\boldsymbol{\nu},\boldsymbol{\mu},t)$. The density matrix can be obtained from the characteristic function using the inversion formula:

$$\rho(\boldsymbol{x},\boldsymbol{x}',t) = \int \frac{\mathrm{d}\boldsymbol{\nu}}{(2\pi\hbar)^3}\, \mathrm{e}^{-\frac{\mathrm{i}}{2\hbar}\boldsymbol{\nu}\cdot(\boldsymbol{x}+\boldsymbol{x}')}\chi(\boldsymbol{\nu},\boldsymbol{x}-\boldsymbol{x}',t). \tag{78}$$

Hence the solution of the master equation (70) is given by:

$$\rho^{\mathrm{cCSL}}(\boldsymbol{x},\boldsymbol{x}',t) = \frac{1}{(2\pi\hbar)^3}\int \mathrm{d}\tilde{\boldsymbol{k}}\int \mathrm{d}\tilde{\boldsymbol{w}}\ \mathrm{e}^{-\frac{\mathrm{i}}{\hbar}\tilde{\boldsymbol{k}}\cdot\tilde{\boldsymbol{w}}}F_{\mathrm{cCSL}}(\tilde{\boldsymbol{k}},\boldsymbol{x}-\boldsymbol{x}',t)\rho^{\mathrm{QM}}(\boldsymbol{x}+\tilde{\boldsymbol{w}},\boldsymbol{x}'+\tilde{\boldsymbol{w}},t), \tag{79}$$

where

$$F_{\mathrm{cCSL}}(\tilde{\boldsymbol{k}},\boldsymbol{q},t) = F_{\mathrm{CSL}}(\tilde{\boldsymbol{k}},\boldsymbol{q},t)\exp\left[\frac{\lambda\bar{\tau}}{2}\left(\mathrm{e}^{-\frac{(\boldsymbol{q}-\frac{\tilde{\boldsymbol{k}}t}{m})^2}{4r_C^2}} - \mathrm{e}^{-\frac{\boldsymbol{q}^2}{4r_C^2}}\right)\right]. \tag{80}$$

For further details about the characteristic function approach see [24, 45]. The interference pattern is given by equation (15) with the function D replaced by $D_{\mathrm{cCSL}} = D_{\mathrm{CSL}}$ given in equation (53). Although F_{CSL} and F_{cCSL} in general differ, i.e. CSL and cCSL have different free evolutions, we have the curious situation that the non Markovian effects in diffraction experiments cancel exactly, i.e. the CSL and cCSL interference patterns coincide.

3.5. QMUPL: quantum mechanics with universal position localization

Here we are referring to the mass-proportional version of the QMUPL model [13, 14]. The single-particle master equation in 3D is given by [44]:

$$\frac{\mathrm{d}\hat{\rho}_t}{\mathrm{d}t} = -\frac{\mathrm{i}}{\hbar}\left[\hat{H},\hat{\rho}_t\right] - \frac{\eta}{2}\frac{m}{m_0}\left[\hat{\mathbf{x}},\left[\hat{\mathbf{x}},\hat{\rho}\right]\right]. \tag{81}$$

In the free particle case, the solution to this master equation can be obtained with the help of the characteristic function:

$$\rho^{\mathrm{QMUPL}}(\boldsymbol{x},\boldsymbol{x}',t) = \frac{1}{(2\pi\hbar)^3}\int \mathrm{d}\tilde{\boldsymbol{k}}\int \mathrm{d}\tilde{\boldsymbol{w}}\ \mathrm{e}^{-\frac{\mathrm{i}}{\hbar}\tilde{\boldsymbol{k}}\cdot\tilde{\boldsymbol{w}}}F_{\mathrm{QMUPL}}(\tilde{\boldsymbol{k}},\boldsymbol{x}-\boldsymbol{x}',t)\rho^{\mathrm{QM}}(\boldsymbol{x}+\tilde{\boldsymbol{w}},\boldsymbol{x}'+\tilde{\boldsymbol{w}},t), \tag{82}$$

where $\rho^{\mathrm{QM}}(\boldsymbol{x},\boldsymbol{x}',t)$ denotes the usual free quantum mechanical evolution ($\eta = 0$) and

$$F_{\mathrm{QMUPL}}(\tilde{\boldsymbol{k}},\boldsymbol{q},t) = \exp\left[\frac{\eta}{2}\frac{m}{m_0}\left[\mathbf{q}^2 - \frac{\mathbf{q}\cdot\tilde{\mathbf{k}}t}{m} + \frac{\tilde{\mathbf{k}}^2}{m^2}\frac{t^2}{3}\right]\right]. \tag{83}$$

The interference pattern is given by equation (15) with the function D defined as follows:

$$D_{\mathrm{QMUPL}}(x_2 - x_2') = \exp\left[-\frac{\eta}{3}\frac{m}{m_0}(t_1+t_2)(x_2-x_2')^2\right]. \tag{84}$$

The function $D_{\mathrm{QMUPL}}(q)$ completely encodes the modification to the quantum mechanical interference pattern ($\eta = 0$).

4. Center-of-mass motion for a rigid object and the amplification mechanism

Matter-wave experiments use large molecules and create spatial superpositions of their center-of-mass motion. In this section, starting from the many-particle collapse dynamics, we will derive a closed equation for the center of mass, under the rigid-body approximation. We will

show and quantify the amplification mechanism: the larger the system, the faster the collapse of the center-of-mass wave function.

We will start by considering the CSL model. Under siutable assumptions, discussed at the end of this section, the analysis applies also to the dCSL, cCSL with small correlation time, and to the DP model. We will discuss three approximations for the geometry of a planar molecule, namely Adler's formula [31], the homogeneous disk approximation and the 2D lattice structure approximation [47].

The N-particle CSL master equation reads:

$$\frac{\mathrm{d}}{\mathrm{d}t}\hat{\rho}(t) = -\frac{\mathrm{i}}{\hbar}\left[\hat{H},\hat{\rho}(t)\right] + \lambda\frac{m^2}{m_0^2}\left(\frac{r_C}{\sqrt{\pi}\hbar}\right)^3 \sum_{j,l}^{N}\int \mathrm{d}\boldsymbol{Q}\, \mathrm{e}^{-\frac{\boldsymbol{Q}^2 r_C^2}{\hbar^2}}\left(\mathrm{e}^{\frac{\mathrm{i}}{\hbar}\boldsymbol{Q}\cdot\hat{\boldsymbol{x}}_j}\hat{\rho}(t)\,\mathrm{e}^{-\frac{\mathrm{i}}{\hbar}\boldsymbol{Q}\cdot\hat{\boldsymbol{x}}_l} - \hat{\rho}(t)\right), \tag{85}$$

where m is the mass of a single particle and $\hat{\boldsymbol{x}}_i$ is the position operator of particle i. By performing a trace over the relative coordinates, we obtain the master equation for the reduced density matrix $\hat{\rho}_{\mathrm{CM}}(t)$ describing the center-of-mass motion:

$$\begin{aligned}\frac{\mathrm{d}}{\mathrm{d}t}\hat{\rho}_{\mathrm{CM}}(t) = &-\frac{\mathrm{i}}{\hbar}\left[\hat{H},\hat{\rho}_{\mathrm{CM}}(t)\right]\\ &+\lambda\left(\frac{r_C}{\sqrt{\pi}\hbar}\right)^3\frac{m^2}{m_0^2}\int \mathrm{d}\boldsymbol{Q}R(\boldsymbol{Q})\,\mathrm{e}^{-\frac{\boldsymbol{Q}^2 r_C^2}{\hbar^2}}\left(\mathrm{e}^{\frac{\mathrm{i}}{\hbar}\boldsymbol{Q}\cdot\hat{\boldsymbol{X}}}\hat{\rho}_{\mathrm{CM}}(t)\,\mathrm{e}^{-\frac{\mathrm{i}}{\hbar}\boldsymbol{Q}\cdot\hat{\boldsymbol{X}}} - \hat{\rho}_{\mathrm{CM}}(t)\right),\end{aligned} \tag{86}$$

where $\hat{\boldsymbol{x}} = \sum_{i=1}^{N}\hat{\boldsymbol{x}}_i/N$ is the center of mass position operator and

$$R(\boldsymbol{Q}) = \int \mathrm{d}\boldsymbol{r}_1 ... \mathrm{d}\boldsymbol{r}_N \sum_{j=1,l=1}^{N} \mathrm{e}^{\frac{\mathrm{i}}{\hbar}\boldsymbol{Q}\cdot(\boldsymbol{r}_j-\boldsymbol{r}_l)} \tag{87}$$

encodes the distribution of atoms in space around the center of mass. By considering a rigid body and neglecting rotations around the center of mass, we can remove the integrations over the relative coordinates [11]:

$$R(\boldsymbol{Q}) = \sum_{j=1,l=1}^{N} \mathrm{e}^{\frac{\mathrm{i}}{\hbar}\boldsymbol{Q}\cdot(\boldsymbol{r}_j-\boldsymbol{r}_l)}. \tag{88}$$

The next step is to replace $R(\boldsymbol{Q})$ with a function independent of the position of the particles, so that equation (86) reduces to a single-particle master equation like equation (50), with λ replaced by an enhanced factor Λ, which depends on the total number of particle and their geometrical distribution. Hence we want to show that under suitable approximations:

$$\lambda\frac{m^2}{m_0^2}\int \mathrm{d}\boldsymbol{Q}R(\boldsymbol{Q})\,\mathrm{e}^{-\frac{\boldsymbol{Q}^2 r_C^2}{\hbar^2}}\,\mathrm{e}^{\frac{\mathrm{i}}{\hbar}\boldsymbol{Q}\cdot\hat{\boldsymbol{X}}}\hat{\rho}_{CM}(t)\,\mathrm{e}^{-\frac{\mathrm{i}}{\hbar}\boldsymbol{Q}\cdot\hat{\boldsymbol{X}}} \longrightarrow \quad \Lambda\int \mathrm{d}\boldsymbol{Q}\,\mathrm{e}^{-\frac{\boldsymbol{Q}^2 r_C^2}{\hbar^2}}\,\mathrm{e}^{\frac{\mathrm{i}}{\hbar}\boldsymbol{Q}\cdot\hat{\boldsymbol{X}}}\hat{\rho}_{CM}(t)\,\mathrm{e}^{-\frac{\mathrm{i}}{\hbar}\boldsymbol{Q}\cdot\hat{\boldsymbol{X}}}, \tag{89}$$

$$-\lambda\frac{m^2}{m_0^2}\left(\frac{r_C}{\sqrt{\pi}\hbar}\right)^3\int \mathrm{d}\boldsymbol{Q}R(\boldsymbol{Q})\,\mathrm{e}^{-\frac{\boldsymbol{Q}^2 r_C^2}{\hbar^2}}\,\hat{\rho}_{CM}(t) \longrightarrow \quad -\Lambda\hat{\rho}_{CM}(t). \tag{90}$$

We now review the three possible methods of approximation mentioned above.

4.1. Adler's formula

Consider first the situation when the molecule is enclosed in a radius $r_s \ll r_C$ (see figure 9). According to equation (86) the weight $\exp(-\boldsymbol{Q}^2 r_C^2/\hbar^2)$ selects those values of $|\boldsymbol{Q}|$ such that $|\boldsymbol{Q}| < \hbar/r_C$. Hence we have that $|\frac{1}{\hbar}\boldsymbol{Q}\cdot(\boldsymbol{r}_j - \boldsymbol{r}_l)| < |\frac{(\boldsymbol{r}_j - \boldsymbol{r}_l)}{r_C}| \approx 0$, and we can write:

$$R(\boldsymbol{Q}) \approx \sum_{j=1,l=1}^{N} 1 = N^2. \tag{91}$$

On the opposite side, let us consider the situation when the distance between nearest neighbour atoms r_a is much bigger than r_C, i.e. $r_C \ll r_a$. We group the terms $\mathrm{e}^{-\boldsymbol{Q}^2 r_C^2/\hbar^2}(\,\mathrm{e}^{\frac{\mathrm{i}}{\hbar}\boldsymbol{Q}\cdot(\boldsymbol{r}_j-\boldsymbol{r}_l)} + \mathrm{e}^{-\frac{\mathrm{i}}{\hbar}\boldsymbol{Q}\cdot(\boldsymbol{r}_j-\boldsymbol{r}_l)})$, which can be rewritten as: $2\mathrm{e}^{-\boldsymbol{Q}^2 r_C^2/\hbar^2}\cos(\boldsymbol{Q}\cdot(\boldsymbol{r}_j - \boldsymbol{r}_l)/\hbar)$. Let us rewrite: $\boldsymbol{Q}\cdot(\boldsymbol{r}_j - \boldsymbol{r}_l) = |\boldsymbol{Q}||\boldsymbol{r}_j - \boldsymbol{r}_l|\cos(\theta)$. Except for the cases when $\cos(\theta) \approx 0$, if $j \neq l$ the condition $r_C \ll r_a$ implies that the oscillations of $\cos(|\boldsymbol{Q}||\boldsymbol{r}_j - \boldsymbol{r}_l|\cos(\theta)/\hbar)$ make the $\boldsymbol{Q}$ integrals negligible. Therefore, the dominant contribution in equation (88) comes from $j = l$ terms, and we can write:

$$R(\boldsymbol{Q}) \approx \sum_{j=1}^{N} 1 = N. \tag{92}$$

The conclusion is that, when N particles in the system are distant less than r_C, we have a quadratic scaling ($\sim N^2$) of Λ for the center of mass motion. On the other hand, when the mutual distance between the N particles is larger than r_C, then Λ for the center of mass motion increases linearly with N.

We also need to consider the intermediate case, where a more careful analysis is needed. In this situation, the behaviour is expected to interpolate between the linear and quadratic scalings. We model the macro-molecules used in the experiments by atoms uniformly distributed over a thin disk, as depicted in figure 9. We neglect the electrons, as their mass is small compared to the nucleon mass and we describe the atomic nuclei as single particles of average mass $m_a = \frac{m}{n_a}$ (average atomic mass), where n_a is the total number of atoms. We limit the discussion to values of r_C larger than the nucleon size $\sim 10^{-15}$ m. The mean area covered by a single atom is πr_a^2, where we take the mean atomic radius to be $r_a = 10^{-10}$ m. The number of atoms contained within a circle of radius r_C is:

$$n(r_C) = \begin{cases} 1, & \text{if } r_C < r_a. \\ \frac{\pi r_C^2}{\pi r_a^2}, & \text{if } r_a \leqslant r_C \leqslant r_s. \\ n_a & \text{if } r_s < r_C. \end{cases} \tag{93}$$

These will contribute quadratically to the collapse rate. The molecule can be covered by $n_a/n(r_C)$ circles of radius r_C and atoms belonging to different circles contribute linearly to the collapse rate. Thus we model the collapse rate for the center of mass of the molecule according to the formula:

$$\Lambda = \frac{n_a}{n(r_C)}\left(\frac{m_a n(r_C)}{m_0}\right)^2 \lambda. \tag{94}$$

This is the formula we will use in following sections. We will describe the center of mass motion as that of a single particle via equation (1), and in all formulas derived starting from it, $\lambda\left(\frac{m}{m_0}\right)^2$ is replaced by Λ. Of course, in the limiting case when the molecular radius r_s is

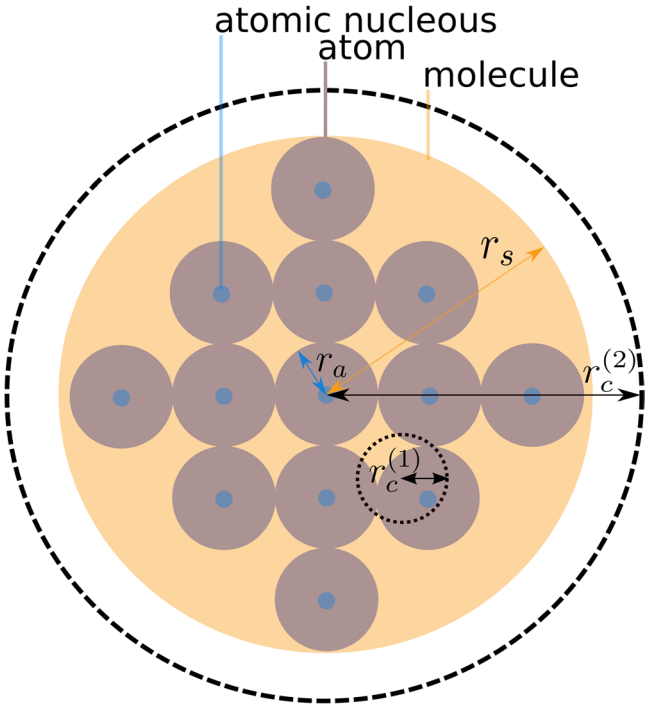

Figure 9. Macro-molecule thin disk approximation with uniformly distributed atoms. The blue circles represent atomic nuclei, the purple circles the atoms of radius r_a and the orange circle of radius r_s denotes the area spanned by the molecule. We assume for simplicity, that the purple circles denoting atoms completely fill the orange circle denoting the molecule, so that empty spaces can be neglected. When $r_C > r_s$, the whole molecule is contained within a circle of radius r_C, and the quadratic scaling law applies (e.g. $r_C = r_C^{(2)}$) . When $r_C < r_a$, only one nucleus is contained within a circle of radius r_C, and the linear scaling law applies (e.g. for $r_C = r_C^{(1)}$). When $r_a < r_C < r_s$, we interpolate the two limiting cases with the scaling law (94).

smaller then r_C, the above scaling reduces to the purely quadratic scaling law, while when the atomic radius r_a is larger than r_C it reduces to the purely linear scaling law. We now discuss two further approximation schemes which will confirm the validity of equation (94).

4.2. Homogeneous thin disk approximation

As a different way to tackle the problem, let us consider the molecule as a thin *homogeneous* disk of radius r_s and thickness d. In this continuous limit, we can approximate:

$$\sum_{j=1}^{N} \mathrm{e}^{\frac{\mathrm{i}}{\hbar}\boldsymbol{Q}\cdot\boldsymbol{r}_j} \quad \longrightarrow \quad \int \mathrm{d}\boldsymbol{x}\rho_{\mathrm{rel}}(\boldsymbol{x})\,\mathrm{e}^{\frac{\mathrm{i}}{\hbar}\boldsymbol{Q}\cdot\boldsymbol{x}} = \tilde{\rho}_{\mathrm{rel}}(\boldsymbol{Q}), \tag{95}$$

where $\rho_{\mathrm{rel}}(\boldsymbol{x})$ is the matter distribution around the center of mass, and $\tilde{\rho}_{\mathrm{rel}}(\boldsymbol{Q})$ its Fourier transform. Then equation (88) reduces to:

$$R(\boldsymbol{Q}) = |\tilde{\rho}_{\mathrm{rel}}(\boldsymbol{Q})|^2. \tag{96}$$

In particular, by labelling the axis of rotational symmetry of the disk as the z axis and its orthogonal plane (x-y plane) with the label o, we find that

$$\tilde{\rho}_{\mathrm{rel}}(\boldsymbol{Q}) = \frac{2\hbar}{Q_o R} J_1\left(\frac{Q_o R}{\hbar}\right) \mathrm{sinc}\left(\frac{Q_z d}{2\hbar}\right), \tag{97}$$

where Q_z,Q_o are the z axis and the x-y plane components of $\boldsymbol{Q}$, respectively and J_1 denotes the Bessel function of the first kind. We now insert $\tilde{\rho}_{\mathrm{rel}}(\boldsymbol{Q})$ into equations (89) and (90) and take the limit $d \to 0$ (very thin disk approximation). To perform the approximation in equation (89) and equation (90), we work in the position basis, i.e. we apply $\langle x, y, z|, |x', y', z'\rangle$ from the left and right, respectively. In addition, we assume that the superposition is on distances much greater than the size of the system, i.e. $\Delta x = x - x'$ is either $|\Delta x| \gg r_s$ or $\Delta x = 0$ and similarly for the y axis. It is then easy to obtain the rescaling of the parameter λ:

$$\Lambda = \frac{4\lambda m^2 r_C^2 \left(1 - \mathrm{e}^{-\frac{r_s^2}{4r_C^2}}\right)}{m_0^2 r_s^2}. \tag{98}$$

4.3. 2D lattice disk

As a different approximation, we consider a 2-D lattice, as depicted in figure 9, of point-like nuclei (small blue circles) forming a thin disk of radius r_s (orange circle). The axis of rotational symmetry of the disk is z, the nuclei sit on the x-y plane and their poisition is denoted as (n_x, n_y). The index n_x runs from $n_{\min} = -\lfloor \frac{r_s}{a} \rfloor$ to $n_{\max} = \lfloor \frac{r_s}{a} \rfloor$, where we take $a = 10^{-10}$ m to be the lattice constant and $\lfloor . \rfloor$ indicates the floor rounded value. Hence the n_y index runs from $-\left\lfloor \sqrt{\frac{r_s^2}{a^2} - n^2} \right\rfloor$ to $\left\lfloor \sqrt{\frac{r_s^2}{a^2} - n^2} \right\rfloor$ in accordance with the circular shape of the molecule $n_x^2 + n_y^2 \leqslant \left(\frac{r_s}{r_a}\right)^2$. In other words, we consider the following $R(\boldsymbol{Q})$ function (88):

$$R(\boldsymbol{Q}) = \sum_{\substack{n_x^2+n_y^2 \leqslant n_{\max}^2 \\ n_x'^2+n_y'^2 \leqslant n_{\max}^2}} \mathrm{e}^{\frac{\mathrm{i}}{\hbar} a(n_x - n_x')Q_x + \frac{\mathrm{i}}{\hbar} a(n_y - n_y')Q_y} \tag{99}$$

where the primed and undprimed variables label the first and second sum, respectively.

Let us first deal with the rescaling in equation (90). We perform the $\mathrm{d}\boldsymbol{Q}$ integration and we get the rescaled parameter Λ:

$$\Lambda = \lambda \sum_{\substack{n_x^2+n_y^2 \leqslant n_{\max}^2 \\ n_x'^2+n_y'^2 \leqslant n_{\max}^2}} \exp\left(-\frac{a^2 (\Delta n_x)^2}{4r_C^2} - \frac{a^2 (\Delta n_y)^2}{4r_C^2}\right) \tag{100}$$

where $\Delta n_x = n_x - n_x'$ and $\Delta n_y = n_y - n_y'$.

Next, we consider the rescaling in equation (89). To ease the analysis, we work in the position basis, i.e. we apply $\langle x, y, z|, |x', y', z'\rangle$ from the left and right, respectively. We consider a single term in equation (99) and perform the $\mathrm{d}\boldsymbol{Q}$ integration in equation (89), we get:

$$\lambda \exp\left(-\frac{(a\Delta n_x + \Delta x)^2}{4r_C^2} - \frac{(a\Delta n_y + \Delta y)^2}{4r_C^2} - \frac{\Delta z^2}{4r_C^2}\right), \tag{101}$$

where $\Delta x, \Delta y, \Delta z$ are $x - x', y - y', z - z'$ respectively. Let us again assume that the superposition varies on distances much greater than the size of the system, i.e. Δx is either $|\Delta x| \gg a\Delta n$ or $\Delta x = 0$. Hence we can approximate $(a\Delta n + \ \Delta \mathrm{x})^2 \approx (a\Delta n)^2 + (\ \Delta \mathrm{x})^2$. A

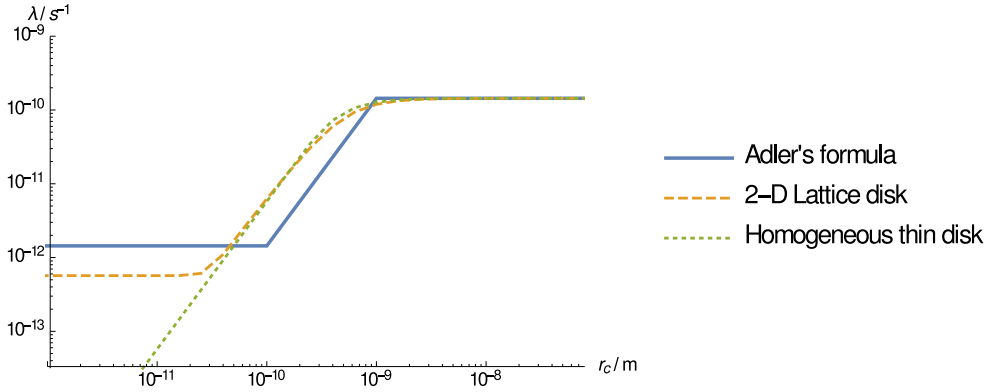

Figure 10. Amplification of the parameter Λ as a function of r_C for three different approximations: Adler's formula (solid blue line), homogenous disk approximation (dotted green line), 2D lattice approximation (dashed orange line). We see, that Adler's formula agrees very well with the more sophisticated 2D lattice model approximation, while the homogenous disk approximation breaks down at distances below the atomic radius ($r_a = 10^{-10}$ m). The plot is obtained for $N = 100$ atoms with atomic (nuclei) mass $12m_0 = 12$ amu.

similar argument can be carried also for the y axis variables. Thus, combining equation (100) and equation (101) we finally obtain:

$$\Lambda \exp\left(-\frac{\Delta x^2 + \Delta y^2 + \Delta z^2}{4r_C^2}\right) - \Lambda, \tag{102}$$

which implies that the center of mass density matrix satisfies the one particle CSL master equation with the rescaled parameter Λ.

4.4. Comparison and other collapse models

The three approximations discussed here above are compared in figure 10. In particular, we see that Adler's heuristic formula is in good agreement with the 2D lattice model amplification mechanism. We also see that the homogeneous thin disk approximation begins to break down for r_C values smaller than the atomic radius r_a as one would expect.

We also stress the key assumption used in the derivation of the amplification mechanism: $r_s \ll r_{\text{sup}}$, where r_s is the size of the system (e.g. molecular radius) and r_{sup} is the size of the macroscopic superposition. Only using this assumption, we were able to effectively describe the center of mass motion master equation (86) by the single particle master equation (50) with the rescaled parameter Λ. When $r_s \gtrsim r_{\text{sup}}$ we have a weaker suppression of macroscopic superpositions.

The dCSL and cCSL models (with small correlation time) many particle master equations have a similar structure as that of the CSL model. Hence, as in part argued in [15, 18], the amplification mechanism is analogous to the CSL amplification mechanism. For the dCSL model, one has to also consider the parameter k_T, which limits the validity of the approximations.

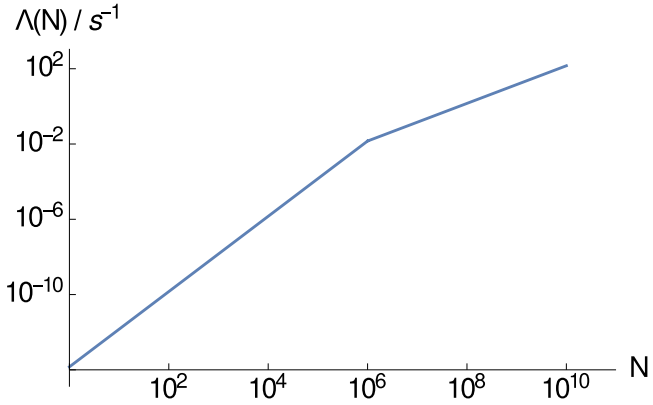

Figure 11. The plot shows the amplification of the effective collapse rate Λ according to equation (94) for the thin disk model described in the text. The plot is obtained with $\lambda = 10^{-16}$ s^{-1}, $r_C = 10^{-7}$ m, atomic radius $r_a = 10$ m and atomic mass $m_a = 12m_0 = 12$ amu. We notice that at $N = 10^6$ the amplification mechanism changes behavior as the total size of the system r_s becomes equal to r_C.

The previous analysis is also applicable to the DP model, as it can be easily shown by considering the many particle DP master equation. As previously stated, in the DP model, R_0 can be identified with r_C and λ can be identified with $\frac{Gm_0^2}{\hbar\sqrt{\pi}R_0}$. As in the CSL model λ rescales to $\Lambda(r_C)$, in the DP model $\frac{Gm_0^2}{\hbar\sqrt{\pi}R_0}$ rescales to $\lambda_{\mathrm{DP}} = \frac{Gm_0^2}{\hbar\sqrt{\pi}R_0}\frac{\Lambda(R_0)}{\lambda}$.

In figure 11 we show how Λ varies as a function of the total number of atoms N according to equation (94), where the atoms form a thin disk lattice structure, as described in figure 9,

The GRW and dGRW models have a simple linear scaling of Λ with the mass of the system by construction.

4.5. Localization requirement of macroscopic objects

In the next section we will derive the upper bounds on the collapse parameters, with reference to the KDTL experiment, but there are also lower bounds, as the collapse cannot be too weak, otherwise the model looses its usefulness. The basic requirement for any collapse model is the rapid suppression of macroscopic superpositions. This type of requirement, which is different in nature from the experimental bounds, has been already considered in [34], where it has been named as the theoretical constraint, and in [33], where it has been called the philosophical constraint. In spite of different names, they are of the same nature.

We make the following reasonable, although arbitrary, minimal request: a macroscopic superposition of an object, visible by the naked eye (with spatial resolution r), should decay within a short time, set by the temporal resolution t of the eye. This implies for example that a macroscopic superposition for a single-layered Graphene disk of radius r localizes with an effective rate t^{-1}. Specifically, we choose the values $t = 10$ ms and $r = 0.01$ mm [48] (for a more refined analysis see [49]).

The quantitative analysis is carried out in the following way. We neglect the free quantum mechanical evolution, while retaining the modification due to the collapse dynamics, i.e. we neglect $\hat{H} = \hat{\boldsymbol{p}}^2/2m$. This is a reasonable assumption since the free quantum mechanical evolution is negligible for macroscopic objects on the time scale during which the wave function

localizes. We have solved the resulting dynamics for each of the collapse models using the characteristic function approach [45]. For each of the considered collapse models the corresponding characteristic function equation is given by:

$$\frac{\partial}{\partial t}\chi(\boldsymbol{\nu},\boldsymbol{\mu},t) = \Lambda\left(\Phi(\boldsymbol{\nu},\boldsymbol{\mu}) - 1\right), \tag{103}$$

where Φ depends on the model. We can easily obtain the solution to this equation:

$$\chi(\boldsymbol{\nu},\boldsymbol{\mu},t) = \chi(\boldsymbol{\nu},\boldsymbol{\mu},0)\exp\left(-\Lambda t(1-\Phi(\boldsymbol{\nu},\boldsymbol{\mu}))\right). \tag{104}$$

Using the inversion formula given by equation (78) we obtain the corresponding density matrix:

$$\rho(\boldsymbol{x},\boldsymbol{x}',t) = \frac{1}{(2\pi\hbar)^3}\int \mathrm{d}\tilde{\boldsymbol{k}}\int \mathrm{d}\tilde{\boldsymbol{w}}\ \mathrm{e}^{-\frac{\mathrm{i}}{\hbar}\tilde{\boldsymbol{k}}\cdot\tilde{\boldsymbol{w}}}\exp\left(-\Lambda t(1-\Phi(\tilde{\boldsymbol{k}},\boldsymbol{x}-\boldsymbol{x}'))\right)\rho(\boldsymbol{x}+\boldsymbol{w},\boldsymbol{x}'+\boldsymbol{w},0), \tag{105}$$

where $\rho(\boldsymbol{x}+\boldsymbol{w},\boldsymbol{x}'+\boldsymbol{w},0)$ is the initial density matrix.

Formally, we can also obtain the solution of the collapse dynamics (without the free quantum mechanical term) from the full solution (with the free quantum mechanical term) by taking the limit $m\to\infty$ in the expressions originating from the free quantum mechanical evolution, while keeping finite m in the other expressions.

We now list the solutions for the considered collapse models using the notation of section 3. For the CSL we obtain:

$$\rho_{\mathrm{CSL}}(\boldsymbol{x},\boldsymbol{x}',t) = \rho(\boldsymbol{x},\boldsymbol{x}',0)\exp\left(-\Lambda t\left(1-\ \mathrm{e}^{-\frac{(\boldsymbol{x}-\boldsymbol{x})^2}{4r_C^2}}\right)\right). \tag{106}$$

The same formula applies also for the cCSL model with small correlation times τ_C.

For the QMUPL we obtain:

$$\rho_{\mathrm{QMUPL}}(\boldsymbol{x},\boldsymbol{x}',t) = \rho(\boldsymbol{x},\boldsymbol{x}',0)\exp\left(-\eta\frac{m}{m_0}t(\boldsymbol{x}-\boldsymbol{x}')^2\right). \tag{107}$$

For the DP we obtain:

$$\rho_{\mathrm{DP}}(\boldsymbol{x},\boldsymbol{x}',t) = \rho(\boldsymbol{x},\boldsymbol{x}',0)\exp\left(-\frac{t}{\hbar}\left(U(\boldsymbol{x}-\boldsymbol{x}')-U(0)\right)\right). \tag{108}$$

For the dCSL we obtain:

$$\rho_{\mathrm{dCSL}}(\boldsymbol{x},\boldsymbol{x}',t) = \frac{1}{(2\pi\hbar)^3}\int \mathrm{d}\tilde{\boldsymbol{w}}\,\rho(\boldsymbol{x}+\tilde{\boldsymbol{w}},\boldsymbol{x}'+\tilde{\boldsymbol{w}},0)$$
$$\int \mathrm{d}\tilde{\boldsymbol{k}}\ \mathrm{e}^{-\frac{\mathrm{i}}{\hbar}\tilde{\boldsymbol{k}}\cdot\tilde{\boldsymbol{w}}}\exp\Big(-\Lambda t(1-\ \mathrm{e}^{-\frac{\tilde{k}^2 r_C^2 k_T^2}{\hbar^2}}\ \mathrm{e}^{-\frac{(\boldsymbol{x}-\boldsymbol{x}')^2}{4r_C^2(1+k_T)^2}}\ \mathrm{e}^{\frac{\mathrm{i}}{\hbar}\frac{2k_T mu}{(1+k_T)}\cdot(\boldsymbol{x}-\boldsymbol{x}')})\Big), \tag{109}$$

where in the limit $k_T\to 0$ we obtain the CSL solution given by equation (106). While for the CSL, cCSL and DP models we were able to perform the $\tilde{\boldsymbol{k}}$ and $\tilde{\boldsymbol{w}}$ integrations, for the dCSL the two integrations in general cannot be performed analytically. Hence for the dCSL we do not have in general a simple exponential decay of the off-diagonal elements. However, we can still investigate the dCSL decay of the off-diagonal elements by considering a particular initial state and performing a numerical simulation. In particular, we have considered a superposition state of two Gaussians centered at points $(r/2,0,0)$ and $(-r/2,0,0)$:

$$\psi(\boldsymbol{x},0)=\left(\exp[-\frac{(x-r/2)^2}{4\sigma^2}]+\exp[-\frac{(x+r/2)^2}{4\sigma^2}]\right)\exp[-\frac{y^2}{4\sigma^2}]\exp[-\frac{z^2}{4\sigma^2}] \tag{110}$$

with r the spatial resolution of the eye and $\sigma=10^{-5}$ m.

For the considered collapse models we can thus write the localization requirement for macroscopic objects as an inequality:

$$\left|\frac{\rho(\boldsymbol{x},\boldsymbol{x}',t)}{\rho(\boldsymbol{x},\boldsymbol{x}',0)}\right|<\exp(-1), \tag{111}$$

where we set $\boldsymbol{x}=(r/2,0,0)$, $\boldsymbol{x}'=(-r/2,0,0)$ and t and r are the eye temporal and spatial resolutions, respectively. The constant $\exp(-1)\sim 0.37$ is chosen arbitrarily, reflecting that for most collapse models the decay of the off-diagonal elements is exponential. This inequality will be used to obtain bounds on collapse parameters.

The same analysis applies also for the GRW and dGRW models, the only difference being the amplification mechanism discussed before.

5. Experimental data analysis

We are now ready to apply the above results to the experiments [36] and [2]. For concreteness, we illustrate the procedure with the CSL model. The same procedure is applicable for each collapse model described in section 3.

In these experiments one has a source of molecules that have different velocities v along the optical axis z. Hence the real far-field interference pattern is given by:

$$\int_0^{+\infty} p_f(v)\,p(x;v)\mathrm{d}v, \tag{112}$$

where p is given by equation (44) and $p_f(v)$ is the macromolecule velocity profile. Similarly the real near-field interference pattern is given by

$$\int_0^{+\infty} p_n(v)S(x_{3s};v)\mathrm{d}v, \tag{113}$$

where S is given by equation (49) and $p_n(v)$ is the macromolecule velocity profile.

To make a quantitative comparison with experimental data, we consider a grid of pairs (λ,r_C) and for each pair we perform a χ^2 minimization procedure for the predicted CSL pattern according to equations (112) and (113). In this way, we obtain a parameter diagram with an exclusion zone of pairs (λ,r_C) that are incompatible with experimental data.

A note of caution is at order. We have initially attempted to fit the experimental data by adopting the Poisson experimental error $\sqrt{I}$ for each value I recorded by the detector since error bars were not reported in the papers. With this choice we were unable to obtain reasonable values of χ^2 even for the standard quantum mechanical predictions. This is probably due, at least in part, to the approximations in the theoretical modeling and to unknown sources of error in the experiment. In order to circumvent this problem and to obtain reasonable values of χ^2, we used an enlarged Poisson experimental error $a\sqrt{I}$, where a is a constant. In order for the standard quantum mechanical fits to have reasonable χ^2 values, we took $a=4.5$ for both experiments, but different values of a (within the same magnitude) do not change the final result.

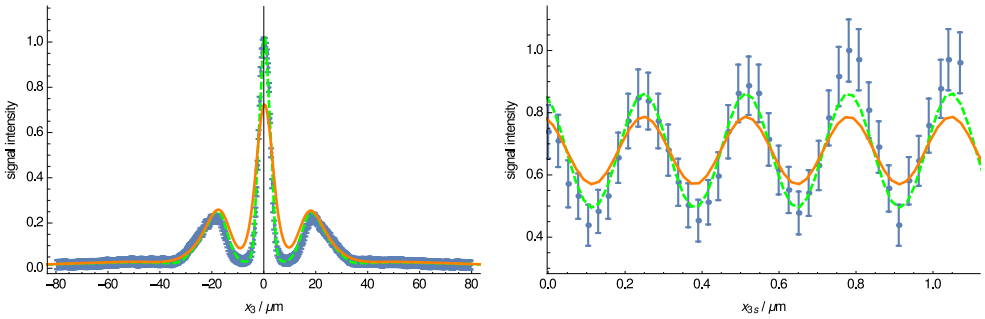

Figure 12. Left: Far-field experiment [36]: $\lambda \approx 3.8 \cdot 10^{-3}$ s^{-1} and $r_C = 10^{-7}$ m. Right: KDTL near-field experiment [2]: $\lambda \approx 0.98 \cdot 10^{-5}$ s^{-1}, $r_C = 10^{-7}$ m, laser power $P_{\text{laser}} = 1$ W. The orange dashed line represents the quantum mechanical fit, the solid orange line represents the CSL fit for an arbitrarily chosen (large) parameter λ and the conventional r_C value and the blue points and blue error bars represent the experimental data. The y axis values are rescaled such that the maximum value is equal to unity.

5.1. Far-field

We first analyze the interference experiment with Phthalocyanine $C_{32}H_{18}N_8$ molecules reported in [1], with the date taken from [36]. The experimental setup is shown in figure 3. The velocity profile was estimated according to [36]. One has to be careful in considering the van der Walls forces between the molecules and the grating. This is modelled by considering an effective slit width smaller than the real one as described in [1]. The effective value is $l_{\text{eff}} = 43$ nm. The finite spatial resolution of the detector 4 μ m was also taken into account.

As an example, in figure 12 we plot a comparison between the experimental interference pattern, the quantum mechanical fit and the CSL fit, for some arbitrarily chosen pair of parameters λ, r_C. More importantly, we repeated the simulation for different pairs of parameters λ, r_C as described before, obtaining the CSL parameter diagram shown in figure 13.

5.2. Near-field KDTL

We now consider the experiment with $L_{12} = C_{284}H_{190}F_{320}N_4S_{12}$ molecules reported in [2]. The experimental setup is shown in figure 3. The Fourier coefficients, defined in equations (45) and (47) for the transmission functions of the mechanical gratings, can be calculated analytically: $A_n = C_n = \frac{2l}{d}\,\text{sinc}(\frac{l}{d}n)$. The velocity profile was approximated by a Gaussian centered around $v = 85$ ms^{-1} with spread $\Delta v_{\text{FWHM}} = 30$ ms^{-1} [2].

As an example, in figure 12 we plot a comparison between the experimental interference pattern, the quantum mechanical fit and the CSL fit, for an arbitrarily chosen pair of parameters λ, r_C. We repeated the simulation for different pairs of parameters λ, r_C as previously described. We obtain the parameter diagram shown in figure 13.

5.3. Comparison of near and far field experiments

Figure 13 shows the exclusion zone of the CSL parameters λ,r_C for the far and near field experiments here considered. As we can see, they are similar: the near-field experiment sets a bound which is roughly two orders of magnitude stronger than the far-field experiment. This can be understood by the following argument.

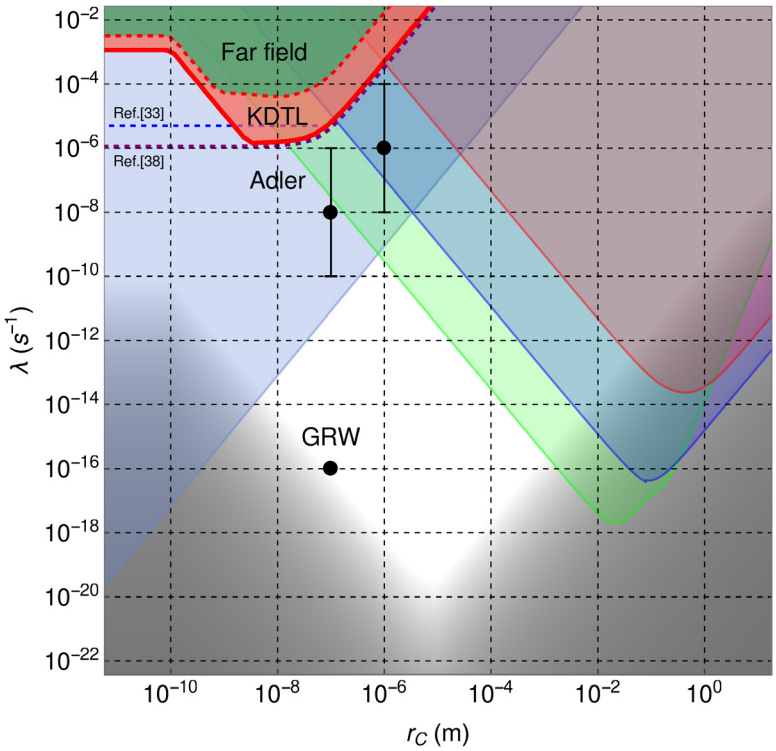

Figure 13. Parameter diagram for the CSL, dCSL and cCSL models. The red shaded zone at the top corresponds to the upper bounds set by the KDTL [2] experiment discussed in the text. We have also reported the bounds from the far field experiment [1, 36], given by the the dark green exclusion zone, which are roughly 2 orders of magnitude weaker. For comparison we have included the bounds from x-ray experiments [50], valid for the CSL model and the cCSL model with frequency cutoff $\Omega \gg 10^{18}$ Hz, given by the light blue exclusion zone on the left, and the bounds from LIGO, LISA Pathfinder and AURIGA [51], analyzed so far for the CSL model only, given by the exclusion zones on the right, shaded in light blue, light green and light red, respectively. The exclusion zone, given by the light gray shaded zone, arises from the requirement of quick suppression of macroscopic superpositions according to the criteria of classicality discussed in the main text. Note that this zone can change significantly depending on chosen criteria of classicality [33, 34], which is reflected by the fuzzy edge of this zone. We have also included for reference, the GRW [12] values $(\lambda = 10^{-16}\ \mathrm{s}^{-1}, r_C = 10^{-7}\ \mathrm{m})$ and the values proposed by Adler [31]: $(\lambda = 10^{-8\pm2}\ \mathrm{s}^{-1}, r_C = 10^{-7}\ \mathrm{m})$ and $(\lambda = 10^{-6\pm2}\ \mathrm{s}^{-1}, r_C = 10^{-6}\ \mathrm{m})$. The dashed blue and purple lines denote the KDTL bounds estimated using the analysis from [33] and [38], respectively. We note that for values of r_C smaller than the size of the macro-molecule ($\simeq 10^{-8}$ m), the bounds on λ become less stringent. Adapted from [39], Copyright (2017), with permission from Elsevier.

Let us fix r_C and focus our attention on the CSL model. The only remaining parameter is λ. We expect that deviations from standard quantum mechanics become important as λt increases. For the far-field experiment we have a typical flight time $t \approx 5$ ms and molecular mass $m \approx 500$ amu. For the near-field experiment we have a typical flight time $t \approx 2$ ms and molecular mass $m \approx 10\,000$ amu. Hence the ratio of bounds on λ from the two experiments is approximately:

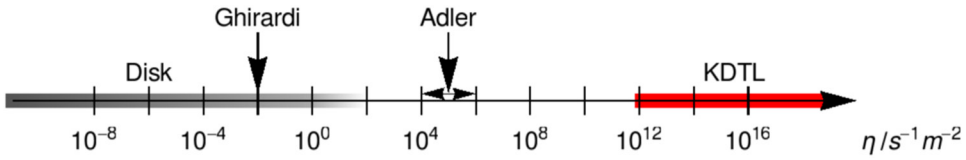

Figure 14. Bounds on the parameter η of the QMUPL model from the KDTL matter-wave interferometry are colored in red. The values colored in gray are excluded from the requirement of quick suppression of macroscopic superpositions: the shade and the fuzzy edge reflect the fact that the excluded interval can vary significantly depending on the chosen criteria of classicality. The excluded zone for the definition of classicality discussed in the main text is $\eta < 10^{1}\ \mathrm{s}^{-1}\ \mathrm{m}^{-2}$ (see also [33, 34]).

$$\frac{\lambda t|_{\mathrm{KDTL}}}{\lambda t|_{\mathrm{far}}} = \frac{(10\,000\ \mathrm{amu})^2\ 2\ \mathrm{ms}}{(500\ \mathrm{amu})^2\ 5\ \mathrm{ms}} \approx 100. \tag{114}$$

This rough estimate provides a simple explanation why the KDTL near-field experiment gives bounds which are 2 order of magnitude stronger than the bounds obtained from the far-field experiment.

5.4. Parameter bounds

The analysis here above refers to the CSL model, but easily applies to the other models discussed in this work. The bounds reported in figure 13 for the CSL model, refer also to dCSL an cCSL. The figure also shows the bounds coming from requiring that macroscopic objects are always well localized (see section 4). This bound puts the original value proposed by GRW right on the border of the exclusion zone (the shaded gray zone at the bottom).

The dCSL bounds from interferometry change slightly if we consider very low temperatures or very high boosts. However, as already stressed before, the smallest modification of the quantum mechanical interference pattern is given by the dCSL model with infinite temperature and no boost, i.e. the CSL model. Hence, since we do not know the temperature and speed of the noise, the most conservative bounds for all dCSL models coincide with the CSL bounds. On the other hand, the bounds obtained by requiring that macroscopic objects are always well localized, become weaker for lower temperatures and higher boost of the noise, but this affects only very high values of r_C. On the other extreme, for very small r_C values, the bounds for dCSL models with very low temperature may become invalid, as the approximations utilized begin to break down. See figures 5 and 6 for a quantitative analysis.

The cCSL bounds from interferometry experiments are valid for noises with a frequency cut-off $\Omega \gg 10^{13}$ Hz. For comparison, bounds from x-ray experiments [50], refer to the cCSL model with a frequency cut-off $\Omega \gg 10^{18}$ Hz. For completeness, we have also shown the CSL bounds from LISA Pathfinder [51].

The fact that the CSL, cCSL and dCSL bounds in figure 13 coincide is due to the fact the time scale of dissipative and non-Markovian effects are longer than the experimental times. This result, shows that interferometric experiments provide bounds that are insensitive to dissipative or non-markavian extensions of the original models for very lage values of the parameters. Interferometric experiments can thus provide a test, not only for a specific model, but for a large class of collapse models, even those not yet considered, such as a CSL model which is both dissipative and non-markovian. For a detailed analysis of the CSL, cCSL and dCSL bounds from non-interferometric experiments with cold-atoms see [52].

The bounds for the GRW and dGRW models can be obtained from the bounds of the CSL and dCSL models, respectively, by changing the amplification factor Λ.

The bounds on the QMUPL model parameter η are shown in figure 14. We can obtain some reference values for the parameter η in the following way: the QMUPL model can be obtained as the limit of the GRW/CSL model [22], specifically, we have $\eta = \lambda/(2r_C^2)$. Using the values suggested in [12] we obtain ($\lambda = 10^{-16}$ s^{-1}, $r_C = 10^{-7}$ m): $\eta_{\mathrm{GRW}} = 10^{-2}$ s^{-1} m^{-2}. We will refer to these value as the Ghirardi values. In [31] we have two different choices: $\lambda = 10^{-8\pm2}$ s^{-1} ($\lambda = 10^{-6\pm2}$ s^{-1}) and $r_C = 10^{-7}$ m ($r_C = 10^{-6}$ m). These give the following value: $\eta_{\mathrm{Adler}} = 10^{5\pm2}$ s^{-1} m^{-2}. We will refer to this value as the Adler value. From figure 14 we see that the Ghirardi value is excluded by the requirement of macroscopic localization.

The KDTL bounds on the DP parameter R_0 fall below the regime of applicability of the DP model ($R_0 \geqslant 10^{-15}$ m). In fact, the effective collapse rate of the DP model $\Lambda_{\mathrm{DP}} = \frac{Gm_0^2}{\hbar\sqrt{\pi}R_0}\frac{\lambda(R_0)}{\lambda}$ is very small above 10^{-15} m, e.g. for $R_0 = 10^{-15}$ m we have $\Lambda_{\mathrm{DP}} \approx 10^{-15}$ s$^{-1}\frac{\lambda(R_0)}{\lambda}$, while for $R_0 = 10^{-7}$ m we have $\Lambda_{\mathrm{DP}} \approx 10^{-23}$ s$^{-1}\frac{\lambda(R_0)}{\lambda}$, which is orders of magnitude below the CSL bounds $\lambda \approx 10^{-3}$ s^{-1}($\lambda \approx 10^{-6}$ s^{-1}) for $r_C = 10^{-15}$ m ($r_C = 10^{-7}$ m), respectively. On the other hand, the requirement that macroscopic objects are always well localized provides very strong bounds. Although these excluded values depend on chosen criteria of classicality [33, 34]), it is nevertheless instructive to make the following estimates. If we require that a single layered Graphene disk of radius $r = 0.01$ mm is to be localized within $t = 10$ ms, as we have done for the CSL family of models, we can already exclude all values of $R_0 = 10^{-15}$ m, $R_0 = 10^{-7}$ m proposed by Diósi [53] and Ghirardi [54], respectively, are still excluded.

Acknowledgments

The authors acknowledge financial support from the EU project NANOQUESTFIT, INFN and FRA 2016 (UNITS). We thank Professor Markus Arndt for the data and the setup parameters of the experiment in [36] and for useful discussions. We also thank Professor Hendrik Ulbricht for many enlightening discussions and Professor Lajos Diósi for comments.

ORCID iDs

Marko Toroš https://orcid.org/0000-0001-8089-8997
Angelo Bassi https://orcid.org/0000-0001-7500-387X

References

[1] Juffmann T, Milic A, Müllneritscha M, Asenbaum P, Tsukernik A, Tüxen J, Mayor M, Cheshnovsky O and Arndt M 2012 Real-time single-molecule imaging of quantum interference *Nat. Nanotechnol.* **7** 297–300
[2] Eibenberger S, Gerlich S, Arndt M, Mayor M and Tüxen J 2013 Matter-wave interference of particles selected from a molecular library with masses exceeding 10000 amu *Phys. Chem. Chem. Phys.* **15** 14696–700
[3] Bell J *et al* 1964 On the Einstein–Podolsky–Rosen paradox *Physics* **1** 195–200
[4] Bell J 2004 *Speakable and Unspeakable in Quantum Mechanics: Collected Papers on Quantum Philosophy* (Cambridge: Cambridge University Press)
[5] Aspect A, Grangier P and Roger Aug G 1981 Experimental tests of realistic local theories via Bell's theorem *Phys. Rev. Lett.* **47** 460–3

[6] Aspect A, Grangier P and Roger G 1982 Experimental realization of Einstein–Podolsky–Rosen–Bohm *Gedankenexperiment*: a new violation of Bell's inequalities *Phys. Rev. Lett.* **49** 91–4

[7] Aspect A, Dalibard J and Roger G 1982 Experimental test of Bell's inequalities using time- varying analyzers *Phys. Rev. Lett.* **49** 1804–7

[8] Bassi A and Ghirardi G C 2003 Dynamical reduction models *Phys. Rep.* **379** 257–426

[9] Bassi A, Lochan K, Satin S, Singh T and Ulbricht H 2013 Models of wave-function collapse, underlying theories, and experimental tests *Rev. Mod. Phys.* **85** 471–527

[10] Pearle P 1989 Combining stochastic dynamical state-vector reduction with spontaneous localization *Phys. Rev.* A **39** 2277–89

[11] Ghirardi G C, Pearle P and Rimini A 1990 Markov processes in Hilbert space and continuous spontaneous localization of systems of identical particles *Phys. Rev.* A **42** 78–89

[12] Ghirardi G C, Rimini A and Weber T 1986 Unified dynamics for microscopic and macroscopic systems *Phys. Rev.* D **34** 470–91

[13] Diósi L 1989 Models for universal reduction of macroscopic quantum fluctuations *Phys. Rev.* A **40** 1165–74

[14] Diósi L 1990 Relativistic theory for continuous measurement of quantum fields *Phys. Rev.* A **42** 5086–92

[15] Smirne A and Bassi A 2015 Dissipative continuous spontaneous localization model *Sci. Rep.* **5** 12518

[16] Bassi A, Ippoliti E and Vacchini B 2005 On the energy increase in space-collapse models *J. Phys. A: Math. Gen.* **38** 8017

[17] Pearle P 1993 Ways to describe dynamical state-vector reduction *Phys. Rev.* A **48** 913–23

[18] Adler S L and Bassi A 2007 Collapse models with non-white noises *J. Phys. A: Math. Theor.* **40** 15083

[19] Adler S L and Bassi A 2008 Collapse models with non-white noises: II. Particle-density coupled noises *J. Phys. A: Math. Theor.* **41** 395308

[20] Bassi A and Ferialdi L 2009 Non-Markovian dynamics for a free quantum particle subject to spontaneous collapse in space: general solution and main properties *Phys. Rev.* A **80** 012116

[21] Ferialdi L and Bassi A 2012 Dissipative collapse models with nonwhite noises *Phys. Rev.* A **86** 022108

[22] Dürr D, Hinrichs G and Kolb M 2011 On a stochastic Trotter formula with application to spontaneous localization models *J. Stat. Phys.* **143** 1096–119

[23] Vacchini B and Hornberger K 2009 Quantum linear Boltzmann equation *Phys. Rep.* **478** 71 - 120

[24] Smirne A, Vacchini B and Bassi A 2014 Dissipative extension of the Ghirardi–Rimini–Weber model *Phys. Rev.* A **90** 062135

[25] Gisin N 1989 Stochastic quantum dynamics and relativity *Helv. Phys. Acta* **62** 363

[26] Percival I C 1994 Primary state diffusion *Proc. R. Soc. Lond.* A **447** 189–209

[27] Hughston L P 1996 Geometry of stochastic state vector reduction *Proc. R. Soc. Lond.* A **452** 953–79

[28] Adler S L, Brody D C, Brun T A and Hughston L P 2001 Martingale models for quantum state reduction *J. Phys. A: Math. Gen.* **34** 8795

[29] Brody D C and Hughston L P 2002 Efficient simulation of quantum state reduction *J. Math. Phys.* **43** 5254–61

[30] Adler S L 2002 Environmental influence on the measurement process in stochastic reduction models *J. Phys. A: Math. Gen.* **35** 841

[31] Adler S L 2007 Lower and upper bounds on CSL parameters from latent image formation and IGM heating *J. Phys. A: Math. Theor.* **40** 2935

[32] Adler S L and Bassi A 2009 Is quantum theory exact? *Science* **325** 275–6

[33] Feldmann W and Tumulka R 2012 Parameter diagrams of the GRW and CSL theories of wavefunction collapse *J. Phys. A: Math. Theor.* **45** 065304

[34] Collett B, Pearle P, Avignone F and Nussinov S 1995 Constraint on collapse models by limit on spontaneous x-ray emission in Ge *Found. Phys.* **25** 1399–412

[35] Collett B and Pearle P 2003 Wavefunction collapse and random walk *Found. Phys.* **33** 1495–541

[36] Sclafani M 2013 Molecular beam methods for quantum optics experiments: sources, detection schemes and coherent manipulation *PhD Thesis* Universität Wien

[37] Nimmrichter S 2014 *Macroscopic Matter Wave Interferometry* (Berlin: Springer) (https://doi.org/10.1007/978-3-319-07097-1)

[38] Nimmrichter S, Hornberger K, Haslinger P and Arndt M 2011 Testing spontaneous localization theories with matter-wave interferometry *Phys. Rev.* A **83** 043621

[39] Toroš M, Gasbarri G and Bassi A 2017 Colored and dissipative continuous spontaneous localization model and bounds from matter-wave interferometry *Phys. Lett.* A **381** 3921–7
[40] Hornberger K, Sipe J and Arndt M 2004 Theory of decoherence in a matter wave Talbot–Lau interferometer *Phys. Rev.* A **70** 053608
[41] Hornberger K 2006 Thermal limitation of far-field matter-wave interference *Phys. Rev.* A **73** 052102
[42] Brezger B, Arndt M and Zeilinger A 2003 Concepts for near-field interferometers with large molecules *J. Opt. B: Quantum Semiclass. Opt.* **5** S82
[43] Pearle P and Squires E 1994 Bound state excitation, nucleon decay experiments and models of wave function collapse *Phys. Rev. Lett.* **73**
[44] Bahrami M, Smirne A and Bassi A 2014 Role of gravity in the collapse of a wave function: a probe into the Diósi–Penrose model *Phys. Rev.* A **90** 062105
[45] Smirne A and Vacchini B 2010 Quantum master equation for collisional dynamics of massive particles with internal degrees of freedom *Phys. Rev.* A **82** 042111
[46] Donadi S, Deckert D-A and Bassi A 2014 On the spontaneous emission of electromagnetic radiation in the CSL model *Ann. Phys.* **340** 70–86
[47] Nimmrichter S, Hornberger K and Hammerer K 2014 Optomechanical sensing of spontaneous wave-function collapse *Phys. Rev. Lett.* **113** 020405
[48] Jacobs G H 2002 Comparative psychology of vision *Handbook of Psychology* (New York: Wiley) ch 3 pp 47–70
[49] Aicardi F, Borsellino A, Ghirardi G C and Grassi R 1991 Dynamical models for state-vector reduction: do they ensure that measurements have outcomes? *Found. Phys. Lett.* **4** 109–28
[50] Curceanu C, Hiesmayr B C and Piscicchia K 2015 X-rays help to unfuzzy the concept of measurement *J. Adv. Phys.* **4** 263–6
[51] Carlesso M, Bassi A, Falferi P and Vinante A 2016 Experimental bounds on collapse models from gravitational wave detectors *Phys. Rev.* D **94** 124036
[52] Bilardello M, Donadi S, Vinante A and Bassi A 2016 Bounds on collapse models from cold-atom experiments *Physica* A **462** 764–82
[53] Diósi L 1987 A universal master equation for the gravitational violation of quantum mechanics *Phys. Lett.* A **120** 377–81
[54] Ghirardi G C, Grassi R and Rimini A 1990 Continuous-spontaneous-reduction model involving gravity *Phys. Rev.* A **42** 1057